

# A Novel Negative Abundance-Oriented Hyperspectral Unmixing Algorithm

Rubén Marrero, Sebastian Lopez, *Member, IEEE*, Gustavo M. Callicó, *Member, IEEE*, Miguel Angel Veganzones, *Member, IEEE*, Antonio Plaza, *Fellow, IEEE*, Jocelyn Chanussot, *Fellow, IEEE*, and Roberto Sarmiento

**Abstract**—Spectral unmixing is a popular technique for analyzing remotely sensed hyperspectral data sets with subpixel precision. Over the last few years, many algorithms have been developed for each of the main processing steps involved in spectral unmixing (SU) under the LMM assumption: 1) estimation of the number of endmembers; 2) identification of the spectral signatures of the endmembers; and 3) estimation of the abundance of end-members in the scene. Although this general processing chain has proven to be effective for unmixing certain types of hyperspectral images, it also has some drawbacks. The first one comes from the fact that the output of each stage is the input of the following one, which favors the propagation of errors within the unmixing chain. A second problem is the huge variability of the results obtained when estimating the number of endmembers of a hyperspectral scene with different state-of-the-art algorithms, which influences the rest of the process. A third issue is the computational complexity of the whole process. To address the aforementioned issues, this paper develops a novel negative abundance-oriented SU algorithm that covers, for the first time in the literature, the main steps involved in traditional hyperspectral unmixing chains. The proposed algorithm can also be easily adapted to a scenario in which the number of endmembers is known in advance and two additional variations of the algorithm are provided to deal with high-noise scenarios and to significantly reduce its execution time, respectively. Our experimental results, conducted using both synthetic and real hyperspectral scenes, indicate that the presented method is highly competitive (in terms of both unmixing accuracy and computational performance) with regard to other SU techniques with similar requirements, while providing a fully self-contained unmixing chain without the need for any input parameters.

Manuscript received November 20, 2013; revised April 10, 2014, July 16, 2014, and November 7, 2014; accepted December 12, 2014. This work was supported in part by the Spanish Ministry of Economy and Competitiveness through the I+D+I Plan 2012–2014 (Research and Development and Innovation) Support Program under the Research Project “Dynamically Reconfigurable Embedded Platforms for Networked Context-Aware Multimedia Systems (DREAMS)” TEC 2011-28666-C04-04 and in part by the European Commission under through the FP7 Future and Emerging Technologies (FET) Funding Program under the Research Project “HypErspectral Imaging Cancer Detection (HELICOID)” under the FP7 Future and Emerging Technologies (FET) funding program, and by XIMRI (ANR 2010 INTB 0208 01) and HYPANEMA (ANR-12-BS03-0003) projects.

R. Marrero is with Institut de Planetologie et d’Astrophysique de Grenoble, Université Joseph Fourier (UJF), CNRS, 38041 Grenoble, France.

S. Lopez, G. M. Callicó, and R. Sarmiento are with the Institute for Applied Microelectronics, University of Las Palmas de Gran Canaria, E-35017 Las Palmas de Gran Canaria, Spain.

M. A. Veganzones is with the Images-Signal Department, GIPSA-Lab, Grenoble Institute of Technology, 38402 Grenoble, France.

A. Plaza is with the Hyperspectral Computing Laboratory, Department of Technology of Computers and Communications, University of Extremadura, E-10003, Cáceres, Spain.

J. Chanussot is with the Images-Signal Department, GIPSA-Lab, Grenoble Institute of Technology, 38402 Grenoble, France.

Color versions of one or more of the figures in this paper are available online at <http://ieeexplore.ieee.org>.

Digital Object Identifier 10.1109/TGRS.2014.2383440

**Index Terms**—Abundance estimation, dimensionality estimation, endmember identification, hyperspectral unmixing, negative abundance-oriented (NABO) algorithm.

## I. INTRODUCTION

SPECTRAL unmixing is an important task in remotely sensed hyperspectral image exploitation [1]. The linear mixture model (LMM) is a widely used technique for spectral unmixing (SU), which is based on the principle that each captured pixel in a hyperspectral image can be represented as the linear combination of a finite set of spectrally pure constituent spectra or endmembers, weighted by an abundance factor that establishes the proportion of each endmember in the pixel under inspection [2]. Hence, under this linear mixing scenario, each pixel of the hyperspectral image can be defined as

$$\mathbf{x} = \mathbf{E}\boldsymbol{\alpha} + \mathbf{n} \quad (1)$$

where  $\mathbf{x}$  is a  $L$ -dimensional vector (with  $L$  being the number of spectral bands of the image),  $\mathbf{E} = [\mathbf{e}_1, \mathbf{e}_2, \dots, \mathbf{e}_p]$  is the endmembers matrix ( $\mathbf{e}_i$  denotes the  $i$ th endmember column vector, with  $p$  being the number of endmembers in the image),  $\boldsymbol{\alpha} = [\alpha_1, \alpha_2, \dots, \alpha_p]^T$  is the abundance vector ( $\alpha_i$  denotes the abundance of the endmember  $\mathbf{e}_i$  in pixel  $\mathbf{x}$ ), and  $\mathbf{n}$  is an additive perturbation (e.g., noise and/or modeling errors) [3]. Due to physical constraints, the abundance vector is nonnegative ( $\boldsymbol{\alpha} \geq 0$ ) and satisfies the sum-to-one constraint ( $\sum_i \alpha_i = 1$ ) [4]. Thus, the geometrical interpretation is that if  $\mathbf{n} = 0$ , each pixel  $\mathbf{x}$  of the image is contained in the simplex whose vertices are the endmembers [5].

In real scenarios, even without perturbation, the magnitude of each pixel of the image is affected by the so-called spectral variability; therefore, it is not possible to ensure that all pixels lie inside the simplex. Spectral variability is due, to a grand extent, to variations in the illumination and atmospheric conditions within a hyperspectral image, causing the spectral signature of a material to vary within an image [6]. If we assume that this spectral variability can be modeled by a scaling factor  $\lambda$ , which is identical for all the endmembers in a given pixel [7], the LMM can be reformulated as

$$\mathbf{x} = \mathbf{E}\boldsymbol{\alpha} + \mathbf{n} \quad (2)$$

where  $\boldsymbol{\alpha} = \lambda\boldsymbol{\alpha}$  holds the positivity constraint but not the sum-to-one constraint. Hence, it is possible to ensure that the pixels lie inside the convex cone defined by  $\mathbf{E}\boldsymbol{\alpha}$  with  $\boldsymbol{\alpha}$  being nonnegative but not sum-to-one constrained.

One of the main benefits of this model when applied on the field of hyperspectral imaging comes from the fact that the number  $L$  of spectral bands is typically much higher than the number  $p$  of endmembers, allowing one to characterize the SU problem in terms of an overdetermined system of equations. More precisely, given a set  $\{e_1, e_2, \dots, e_p\}$ , the SU problem consists in finding the abundance coefficients  $\{a_1, a_2, \dots, a_p\}$  such that the distance  $\|\mathbf{E}\mathbf{a} - \mathbf{x}\|_2$  is minimized. The unconstrained solution to this problem is given by

$$\mathbf{a} = \mathbf{E}^+ \mathbf{x} \quad (3)$$

being  $\mathbf{E}^+ = (\mathbf{E}^T \mathbf{E})^{-1} \mathbf{E}^T$  the Moore–Penrose pseudoinverse of  $\mathbf{E}$  [8].

In the following, (3) indicates the SU solution according to model (2), in which the nonnegativity and sum-to-one constraints have been relaxed. This solution will be denoted from now on as the unconstrained abundances.

Within the linear unmixing paradigm, up to three types of unmixing algorithms can be identified: geometrical, statistical, and sparse algorithms [1]. Geometrical unmixing algorithms work under the assumption that the endmembers of a hyperspectral image are the vertices of a geometrical figure that is maximally contained [9]–[11] or minimally encloses [12]–[14] the data in the targeted hyperspectral image. As their name suggests, statistical methods [15], [16] are based on analyzing mixed pixels by means of statistical principles, such as Bayesian approaches [17]. Finally, sparse regression-based algorithms are based on expressing each mixed pixel in a scene as a linear combination of a finite set of pure spectral signatures that are *a priori* known [18], [19]. Although each of these methods exhibits their own pros and cons, the fact is that geometrical approaches have been the ones most frequently used by the hyperspectral research community up to now [1]. This is mainly due to their reduced—although still high—computational cost when compared with the other types of unmixing algorithms, as well as to the fact that they represent a straightforward interpretation of the linear model as defined in (1).

To fully unmix a given hyperspectral image by means of a geometrical method, the majority of the state-of-the-art approaches are based on dividing the whole process into three concatenated steps: 1) estimate the number of endmembers that are present in the image under analysis; 2) induce these endmembers from the data; and 3) calculate per each mixed pixel of the image the abundances associated with the endmembers already computed. This is summarized in Fig. 1, where a *de facto* hyperspectral unmixing chain is depicted.

Although this strategy has proven to be effective for unmixing certain types of hyperspectral images, it also has associated three main inherent drawbacks.

- 1) The first one comes from the fact that the output of each stage is the input of the following one, which favors the propagation of errors within the unmixing chain.
- 2) The second one becomes determined by the huge variability of the results obtained when estimating the number of endmembers of a hyperspectral scene with different state-of-the-art algorithms, or in some cases, with the same algorithm but with different initialization parameters. For

instance, if the number of endmembers is obtained by means of computing the virtual dimensionality (VD) of the image, very different results may be obtained depending on the technique employed for estimating the VD itself [20]. Furthermore, even when the same technique is employed, dissimilar results may be achieved for different values of the false-alarm probability  $P_F$ , which should be mandatory fixed to a certain (unknown) value to estimate the VD of an image through the Harsanyi–Farrand–Chang (HFC) or noise-whitened HFC (NWHFC) methods [8]. Finally, it is worth to mention that different works [21] have already uncovered that, for a given hyperspectral image, the number of endmembers obtained by estimating the VD of the targeted image may significantly differ from the one obtained with other well-known algorithms, such as the hyperspectral signal identification by minimum error (HySime) algorithm [22]. Moreover, some other algorithms that have been recently proposed in the literature [23], [24], have demonstrated to provide results that differ from those achieved with the VD and the HySime techniques, which add even more uncertainties to the process of accurately estimating the number of endmembers of a hyperspectral image.

- 3) Finally, the third drawback refers to the circumstance that all the possible combinations of algorithms to fully unmix a hyperspectral image demand a formidable computational effort, this effort being typically higher if better unmixing performance of the designed unmixing chain is needed.

In this paper, we develop a novel abundance-guided unsupervised algorithm that addresses the three previously identified drawbacks. The proposed algorithm selects the pixels lying outside the hypercone defined by a set of candidate endmembers as better candidates; thus, we call it negative abundance-oriented (NABO) algorithm.

Recently, methods based on estimated abundance to guide the endmember induction process have been proposed [30], [31]. These methods assume that the pixels with highest abundance absolute values for some set of candidate endmembers are better candidates to be the actual endmembers. For a given number of endmembers, these methods start with a set of candidate endmembers and then estimate the fractional abundance according to the LMM, using the sum-to-one but not the nonnegativity constraint. An iterative process selects the pixel with the highest abundance component in absolute value as a new candidate endmember. This new candidate endmember replaces the old one corresponding with the maximum abundance component index. Then, the fractional abundances are reestimated, and the iterative process continues until the fractional abundance component with maximum absolute value falls below a tolerance threshold. These methods are fast but also sensitive to outliers. In [30], a spatial information process is proposed based on the assumption that the purest signatures are usually distributed in spatially homogeneous areas to overcome the outlier-related issues.

The main differences between the proposed NABO algorithm and the aforementioned abundance-guided methods [30], [31] are the following.

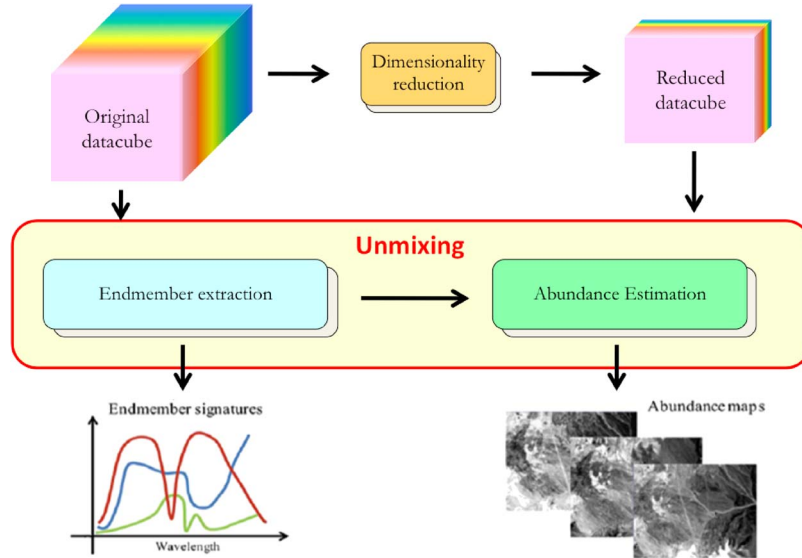


Fig. 1. De facto hyperspectral unmixing processing chain.

- We propose a methodology to introduce the estimation of the number of endmembers as an inherent part of the unmixing process. This is based on the error between the original image and the reconstructed one using the unconstrained abundances; therefore, the error can only be explained in terms of noise and lack of dimensionality.
- The proposed NABO method imposes no constraints to the abundance estimation, and the search is guided by the maximum negativity; whereas, in [30] and [31], sum-to-one constraint is imposed and the search is guided by the maximum absolute value. Both criteria are similar since a high absolute value (greater than one) with sum-to-one constraint implies negative abundance of at least one of the components of the abundance vector. The reason why we do not consider the sum-to-one constraint is twofold. On one hand, we do not need it to guide the search since the criterion is based on identifying those pixels lying outside the hypercone defined by the candidate endmembers, i.e., negativity is a necessary and sufficient criterion. On the other hand, normalizing the abundances introduces another source of error in the process of estimating the number of endmembers since the length of the reconstructed pixels is modified.
- We propose the use of a global objective function in NABO to identify the substituted endmember, in contrast with [30] and [31], where no criteria are followed. This global function avoids the selection of outliers as candidate endmembers and offers a more straightforward stopping rule than the *a priori* selection of a tolerance value.
- In addition, we propose a more conservative methodology to select the new candidate endmember and the old endmember that the new endmember will substitute. In [30] and [31], the pixel with maximum absolute abundance is selected to substitute the endmember corresponding to the index of such abundance. The proposed NABO methodology selects a set of candidate pixels ordered by maximum

negative abundance. NABO proceeds by selecting the first candidate pixel and testing all the possible substitutions. The substitution that most improves the global objective function is retained. If no substitution improves the objective function, the pixel is discarded, and the next candidate pixel is selected. The process follows up to a number of candidate pixels indicated by an exhaustivity counter. However, we have experimentally check that, in most cases, when a substitution happens, the substituted endmember corresponds to an abundance with high absolute value; therefore, the criterion followed in [30] and [31] is a good heuristic to the selection of the substitution.

As it will be further detailed, our algorithm is capable to effectively obtain the number of the endmembers of the image, to induce these endmembers, and to compute their corresponding unconstrained abundances without splitting the process into the three different computing stages. Thus, each of the estimation processes (involving the number of endmembers, the endmembers themselves, and the unconstrained abundances) make use of the information provided by the other two, providing a feedback that prevents the propagation of errors. Summarizing, the proposed algorithm prevents the propagation of errors by interlacing the three SU stages, gives a robust estimation of the number of endmembers, and presents a computational burden comparable to fast state-of-the-art methods, i.e., vertex component analysis (VCA) [5].

To compare its performance with respect to other existing algorithms, the proposed algorithm can be also configured to only extract the endmembers of an image together with their associated unconstrained abundances once the number of endmembers present at the targeted hyperspectral scene has been indicated as an input parameter. The results obtained with synthetic and real remotely sensed hyperspectral images demonstrate the benefits provided by our NABO algorithm due to the fact that it is based on analyzing the negativity of a set of previously computed unconstrained abundances. Furthermore, the endmember induction performance of NABO is compared

against the method proposed in [30]. In this comparison, we illustrate that NABO is less sensitive to outliers than the method in [30] when no spatial information is taken into account, highlighting the relevance of the proposed NABO global objective function.

The remainder of this paper is organized as follows. Section II details the fundamentals of the proposed NABO algorithm. Section III introduces two additional algorithms that are based on the same principles than NABO but include some further preprocessing operations to reduce its spectral dimensionality and therefore reduce the noise of the image under analysis and the time required to unmix the image. Section IV presents the most significant results obtained with all the proposed algorithms with synthetic and real hyperspectral images, comparing their performances with different state-of-the-art approaches. Section V outlines the most important concluding remarks extracted from this paper and provides hints at plausible future research lines.

## II. PROPOSED NABO UNMIXING ALGORITHM

The proposed NABO algorithm consists in exploiting the unconstrained abundance information in a geometrical greedy fashion to obtain suboptimal solutions for the complete SU problem: the determination of the number  $p$  of endmembers, the extraction of these endmembers  $\{e_1, e_2, \dots, e_p\}$ , and the estimation of the unconstrained abundance  $\{a_1, a_2, \dots, a_N\}$  for every pixel of the image, with  $N$  being the total number of pixels.

NABO is based on three main principles.

- 1) The first one is pure-pixel assumption, i.e., the presence of pure spectra in the data.
- 2) The second one refers to the issue that unconstrained abundances are useful to determine the actual number of endmembers that constitute a hyperspectral image as it will be demonstrated in this paper. More concretely, it takes advantage of the fact that if the estimated number  $\hat{p}$  of endmembers is underestimated, i.e.,  $\hat{p} < p$ , the error between the original image and the reconstructed image will be higher than a given threshold. This will be explained in detail in Section II-A.
- 3) The third one consists of directing the algorithm search for the best candidates to be actual endmembers by analyzing the negativity of the calculated unconstrained abundances for a given set of pixels as candidate endmembers. In this way, NABO makes possible to reach a suboptimal solution without performing an exhaustive search. This second principle will be detailed in Section II-B.

### A. Estimation of the Number of Endmembers

Assuming the linear model (1) with zero-mean Gaussian white noise and a given set of  $\hat{p}$  candidate endmembers  $\hat{\mathbf{E}} = [\hat{e}_1 \hat{e}_2 \dots, \hat{e}_{\hat{p}}]$  as a  $L \times \hat{p}$  matrix, the reconstruction of the  $j$ th pixel is given by

$$\hat{\mathbf{x}}_j = \sum_{i=1}^{\hat{p}} \hat{e}_i \hat{a}_{ij} \quad (4)$$

with  $\hat{a}_{ij}$  as the unconstrained abundances obtained by

$$\hat{\alpha}_j = \hat{\mathbf{E}}^+ \mathbf{x}_j. \quad (5)$$

Thus, the associated reconstruction error vector is given by

$$\varepsilon_j = \mathbf{x}_j - \hat{\mathbf{x}}_j = \sum_{i=1}^p e_i a_{ij} + \mathbf{n}_j - \sum_{k=1}^{\hat{p}} \hat{e}_k \hat{a}_{ij} \quad (6)$$

with  $e_i$  being the actual  $i$ th endmember,  $a_{ij}$  being the actual abundance of the  $i$ th endmember in the  $j$ th pixel,  $p$  being the actual number of endmembers, and  $\mathbf{n}_j$  being the noise vector associated to the  $j$ th pixel.

Hence, the mean power reconstruction error of the image can be defined as

$$P_{\text{error}} = \frac{1}{NL} \sum_{k=1}^L \sum_{j=1}^N \varepsilon_{kj}^2 \quad (7)$$

where  $N$  is the number of pixels, and  $L$  represents the number of spectral bands of the hyperspectral image. Expanding (7) and assuming that

$$\hat{e}_{ki} = e_{ki} + n_{ki} \quad (8)$$

i.e., the  $i$ th induced endmember is the  $i$ th actual endmember obtained as a noisy pixel of the image, the following equation is obtained:

$$P_{\text{error}} = \frac{1}{NL} \sum_{k=1}^L \sum_{j=1}^N \left( \sum_{i=1}^p e_{ki} a_{ij} - \sum_{i=1}^{\hat{p}} e_{ki} \hat{a}_{ij} + n_{kj} - \sum_{k=1}^{\hat{p}} n_{ki} \hat{a}_{ij} \right)^2. \quad (9)$$

Let us denote by  $\eta_{kj}^p = \sum_{i=1}^p e_{ki} a_{ij} - \sum_{i=1}^{\hat{p}} e_{ki} \hat{a}_{ij}$  the error due to the underestimation of the number of endmembers; similarly, let us denote by  $\eta_{kj}^e = \sum_{i=1}^{\hat{p}} n_{ki} \hat{a}_{ij}$  the error due to the endmembers noise in the image and by  $n_{kj}$  the noise of the image. Then,  $P_{\text{error}}$  can be written as

$$P_{\text{error}} = \frac{1}{NL} \sum_{k=1}^L \sum_{j=1}^N \eta_{kj}^p{}^2 + n_{kj}^2 + \eta_{kj}^e{}^2 - 2n_{kj} \eta_{kj}^e + 2\eta_{kj}^p (n_{kj} - \eta_{kj}^e). \quad (10)$$

At this point, we have on the one hand

$$\begin{aligned} \frac{1}{NL} \sum_{k=1}^L \sum_{j=1}^N n_{kj} \eta_{kj}^e &= E[n_{kj} \cdot \eta_{kj}^e] \\ &= E[n_{kj}] \cdot E[\eta_{kj}^e] + \text{cov}(n_{kj}, \eta_{kj}^e) \approx 0 \end{aligned} \quad (11)$$

because  $n$  is zero-mean Gaussian white noise. On the other hand, if  $\hat{p} = p$ , we have

$$\eta_{kj}^p = 0 \quad (12)$$

hence

$$P_{\text{error}} \approx \frac{1}{NL} \sum_{k=1}^L \sum_{j=1}^N n_{kj}^2 + \frac{1}{NL} \sum_{k=1}^L \sum_{j=1}^N \eta_{kj}^e = P_x + P_{\eta^e}. \quad (13)$$

Using any noise estimator such as the one proposed in [22], it is possible to estimate  $P_x$  and  $P_{\eta^e}$ , reaching the desired criterion

$$P_{\text{error}} \leq P_x + P_{\eta^e} \quad (14)$$

which means that, if  $P_{\text{error}} > P_x + P_{\eta^e}$ , this implies that  $\hat{p} < p$ , i.e., the number of endmembers is underestimated.

Thus, the quality of the noise estimation affects the performance of the number of endmembers estimated by (14). On the one hand, if the estimated noise is greater than the actual noise, this could result in an underestimated number of endmembers since the stop criteria could be matched by a lower dimensionality error. On the other hand, if the estimated noise is lower than the actual noise, the number of endmembers could be overestimated since it could be necessary a larger set of endmembers to reduce the reconstruction error. Furthermore, the quality of the induced endmembers does not seriously affect (14) if the induced endmembers are linear combinations of the set of actual endmembers since it is always possible to reconstruct the image pixels from a linear combination of the set of actual endmembers.

### B. Endmembers Induction Criterion Based on Abundance Negativity

The main idea of NABO is inducing the endmembers from the image based on a negative abundance criterion so that the algorithm does not need to perform an exhaustive search. Given a set of candidate endmembers, all the pixels that lie outside the hypercone defined by these endmembers have necessarily a negative abundance. Hence, pixels with a negative abundance are alternative candidates to be endmembers. In fact, pixels with the highest negative abundances are the best candidates to be the sought endmembers.

Let us assume a toy example in which the pixel  $x$  is given by

$$x = \sum_{i=1}^p e_i a_i \quad (15)$$

where  $e_i$  is the  $i$ th actual endmember, and  $a_i$  is the nonnegative abundance of the  $i$ th endmember in pixel  $x$ , which lies inside the hypercone defined by endmembers  $e_i$ . If  $e_1$  is expressed in terms of the other endmembers and  $x$ , the following expression is obtained:

$$e_1 = \frac{1}{a_1} x + \sum_{i=2}^p \frac{-a_i}{a_1} e_i. \quad (16)$$

Due to the nonnegativity of the abundances  $a_i$ , the terms  $-a_i/a_1$  are negative; therefore  $e_1$  lies outside the hypercone defined by the remaining set of endmembers and the pixel  $[e_2, e_3, \dots, e_p, x]$ . Moreover, the further  $e_1$  is from  $x$ , the smaller  $a_1$  is; therefore, terms  $-a_i/a_1$  are more negative, show-

ing that negative abundances are a good indicator to select candidate endmembers.

At this point, it should be noted that other methods such as those in [30] and [31] perform the search for endmember candidates guided by the maximum absolute value of the estimated abundances because they apply sum-to-one constraint to these abundances. Both criteria are similar since a high absolute value (greater than one) with sum-to-one constraint implies negative abundance of at least one of the components of the abundance vector. For instance, it is shown in (16) that the term  $1/a_1$  increases, whereas  $a_1$  decreases, which could be also a good criterion if applying sum-to-one constraint (normalizing) to fairly compare these values. However, the need of unconstrained abundances by our approach for estimating the number of endmembers and some particularities of the NABO algorithm that will be explained in the following led us to use a strategy different to the one adopted in [30] and [31].

### C. Implementation of the Proposed Algorithm

To induce the set of endmembers that makes a better characterization of the hyperspectral image under analysis in terms of the LMM, this paper proposes an iterative process guided by the minimization of the following global energy objective function, where  $j$  keeps track of every pixel in the image:

$$\arg \min_{\mathbf{E}} J(\mathbf{E}); \quad J = \left| \sum_j \beta_j \right| \times \beta_j \begin{cases} \min_i(a_{ij}) & \text{if } \min_i(a_{ij}) < 0 \\ 0 & \text{if } \min_i(a_{ij}) \geq 0. \end{cases} \quad (17)$$

Solving (17) is a fast, simple, and light process to induce the set of endmembers based on the negativity of the abundances at each pixel. Hence, the algorithm tries to find the more outward pixels enclosing as many pixels as possible inside its associated hypercone. In noisy scenarios, including all the pixels inside the hypercone is not possible, i.e., there is no pixel without negative unconstrained abundance of at least one endmember. However, the algorithm looks for the closest solution that minimizes the abundance negativity of the pixels of the image.

Hence, the algorithm consists of a refinement where the unconstrained abundances are fed back while the set of pixels assumed as endmembers are continuously replaced by the best pixel candidates, trying to minimize the objective function, and while the numbers of endmembers is increased until a suitable number of endmembers is reached. Furthermore, the algorithm is unsupervised, unless for the inferior and superior limits defined for the number of endmember estimation and for an exhaustiveness counter variable that the user defines as an input of the algorithm.

Algorithm 1 shows the pseudocode of the proposed NABO algorithm. The algorithm starts with a preprocessing step where the image noise is estimated using a technique presented in [22]. Then, variable  $\mathbf{p}$  is initialized to an underestimated  $\mathbf{p}_{\text{init}}$  value; and  $\mathbf{p}$  pixels are chosen to be the initial endmembers.

**Algorithm 1** Pseudocode of NABO algorithm

**INPUTS:**  $p\_init$ ,  $p\_end$ , **exhaustivity\_counter**,  $\mathbf{X} = [\mathbf{x}_1, \mathbf{x}_2, \dots, \mathbf{x}_N]$ ;  $X$  is composed by  $N$  hyperspectral pixels

**1: Preprocessing**

- No dimensional reduction.
- Noise estimation for stopping rule.
- Initialize  $p$  to the  $p\_init$  value.
- Let  $\{\mathbf{e}_1, \mathbf{e}_2, \dots, \mathbf{e}_p\}$  be a set of initial vector randomly selected (or as input) from  $\mathbf{X}$ .

**2: Initialization**

- Initialize **counter** to the **exhaustivity\_counter** value.
- Calculate the unconstrained abundances of every pixel of the image with the set of endmembers  $\{\mathbf{e}_i\}$   $i = 1$  to  $p$ .
- Calculate the energy  $J$  of the objective function by using the unconstrained abundances.
- Update the **best\_candidates\_list** through the negativity of the unconstrained abundances. The pixel with the most negative abundance is the best candidate; the pixel with the second most negative abundance is the second best candidate; ...

**3: Outer Loop** ( $j$  keeps track of the  $j$ th best candidate)

- Take  $\mathbf{r}$  as best candidate currently: take the  $j$ th element of **best\_candidates\_list**.

**4: Inner Loop** ( $i$  keeps track of the  $i$  endmember  $\mathbf{e}_i$ ,  $1 < i < p$ )

- Calculate the unconstrained abundances for  $\{\mathbf{e}_1, \mathbf{e}_2, \dots, \mathbf{e}_{i-1}, \mathbf{r}, \mathbf{e}_{i+1}, \dots, \mathbf{e}_p\}$  if this set of vector is linearly independent.
- Calculate the energy  $J_i$  of the objective function by using the unconstrained abundances.

**5: Replacement rule**

- Once the algorithm exits from the Inner Loop, if any of the calculated energy ( $J_i$ ) of the objective function is lesser than the energy obtained by  $\{\mathbf{e}_i\}$   $i = 1$  to  $p$  then
- The replacement is performed, so the new set of end-members is  $\{\mathbf{e}_1, \mathbf{e}_2, \dots, \mathbf{e}_{i-1}, \mathbf{r}, \mathbf{e}_{i+1}, \dots, \mathbf{e}_p\}$
- **counter** = **exhaustive\_counter**
- Update the **best\_candidates\_list** through the negativity of the unconstrained abundances. The pixel with most negative abundance is the best candidate, the pixel with the second most negative abundances is the second best candidate, ...
- Initialize  $j = 1$ .
- Go to Step 3.

**6: Exhaustivity counter decrementation**

- **counter** is decremented by one.
- If counter does not reach 0, go to Step 3.

**7: Stopping rule**

- Calculate the reconstructed image by multiplying the current set of endmembers and its associated unconstrained\_abundances.
- If the reconstruction error power is smaller than the criterion exposed in Section II or  $p$  is equal to  $p\_end$ , then go to Step 8.
- If not, increment  $p$  by one unit and update the end-members including  $\mathbf{e}_p$ , as the best candidate (first element of **best\_candidates\_list**).
- Go to Step 2.

**8: Exit**

- If we do not want noiseless endmembers then **end**.
- Obtaining  $U_p$  by PCA.
- $\mathbf{Y} = \mathbf{U}_{p-1}^T \mathbf{U}_{p-1} (\mathbf{X} - \bar{\mathbf{X}}) + \bar{\mathbf{X}}$
- $\mathbf{E} = \mathbf{Y}_{:, E\_index}$  (index is the vector with the endmember index position in the image).

**OUTPUT:**  $\mathbf{E} = [\mathbf{e}_1, \mathbf{e}_2, \dots, \mathbf{e}_p]$ , **unconstrained Abundances A**

After that, the algorithm reaches the initialization step where the **counter** variable is initialized to the **exhaustivity\_counter** given by the user. This counter tracks the exhaustiveness of the endmember search procedure. Furthermore, the algorithm calculates the unconstrained abundances of the endmembers for every pixel of the image. With these unconstrained abundances, the energy  $J$  is calculated. In addition, the unconstrained abundances allow to construct the **best\_candidates\_list** vector through the negativity of the abundances, due to the fact that the pixels with the most negative abundances are the best candidates to be considered as endmembers, as it has been shown in the earlier section. Hence, the pixel with the most negative abundance is the best candidate, the pixel with the second most negative abundance is the second best candidate, and so on.

Steps 3 and 4 reflect the iterative nature of the algorithm, trying to find a suboptimal solution without conducting an exhaustive search where the outer loop runs on pixels indexed in **best\_candidates\_list** vector, whereas the inner loop is used to check if there is a need to have one of the current  $p$  endmember replacement by the currently pixel chosen in the outer loop, e.g.,  $\mathbf{r}$ . The inner loop checking process consists of calculating  $J$  by means of the unconstrained abundances of endmembers, replacing each endmember by  $\mathbf{r}$  in each iteration.

Hence, if one of the calculated  $J$  energy values in the inner loop is smaller than the current minimum  $J$  energy, the replacement is performed, the **counter** variable is initialized to the **exhaustive\_counter** value, the **best\_candidates\_list** vector is updated, and the algorithm returns to the outer loop. On the contrary, if none of the calculated  $J$  energy values in the inner loop is smaller than the current minimum  $J$  energy, the **counter** variable is decremented by one.

If **counter** reaches a value equal to zero, the algorithm checks if the stopping rule is met. If it does, the algorithm finalizes. Otherwise, the algorithm returns to the initialization step after incrementing  $p$  by one unit and adding the first element of **best\_candidates\_list** to the set of endmembers.

Regarding the reason why we did not follow the overall strategy presented in [30] and [31], it is important to highlight that we have experimentally found that using the absolute value criterion with sum-to-one constraint instead of the unconstrained negativity criterion in NABO yields to multiple selections of the same pixel as candidate endmembers when underestimating the actual number of endmembers, undermining the ability of the NABO method to induce endmembers and accurately estimate the actual endmember number. Hard coding as a solution to this issue will introduce unnecessary complexity. In addition, avoiding normalizing the abundances lightens the computational burden, although we are aware that this criterion slightly promotes pixels with high magnitude for two reasons: i) For a given pixel and a given set of candidate endmembers, the higher the magnitude of the pixel the higher the absolute value of the unconstrained abundances; and ii) regarding the objective function, the abundances of all the pixels of the image with respect to this candidate endmember with high magnitude will be lower than the abundances obtained with the same candidate endmember with shorter length.

### III. FURTHER IMPLEMENTATIONS

To increase the performance of the proposed NABO algorithm, two optional steps have been included to reduce noise of the hyperspectral image under processing and the execution time of the NABO algorithm, respectively. These two alternative implementations have been developed taking into account the principal component analysis (PCA) preprocessing stage that can be found in different endmember extraction algorithms, such as the vertex component analysis (VCA) [5].

On the one hand, the first implementation called NABO NO NOISE (NABO\_NN) consists of projecting the data as  $Y = U_{p-1}^T U_{p-1}(X - \bar{X}) + \bar{X}$ , with  $U_{p-1}$  being the first  $p-1$  components of the  $L \times (p_{end}-1)$  matrix obtained by PCA,  $X$  being the original data  $L \times N$  matrix, and  $\bar{X}$  being the sample mean vector  $L \times 1$  of  $X$ . Thus, the proposed algorithm works on an input noiseless hyperspectral data set, being this projection performed every time that the variable  $p$  is increased. The pseudocode of this alternative implementation can be found in Algorithm 2.

---

#### Algorithm 2 Pseudocode of NABO\_NN algorithm

---

**INPUTS:**  $p_{init}$ ,  $p_{end}$ , **exhaustivity\_counter**,  $X = [x_1, x_2, \dots, x_N]$ ;  
 $X$  is composed by  $N$  hyperspectral pixels

##### 1: Preprocessing

- Noise estimation for stopping rule.
- Obtaining  $U_{p_{end}}$  by PCA.
- Initialize  $p$  to the  $p_{init}$  value.
- $Y = U_{p-1}^T U_{p-1}(X - \bar{X}) + \bar{X}$
- Let  $\{e_1, e_2, \dots, e_p\}$  be a set of initial vector randomly selected (or as input) from  $Y$ .

##### 2: Initialization

- Initialize **counter** to the **exhaustivity\_counter** value.

- Calculate the unconstrained abundances of every pixel of the image with the set of endmembers  $\{e_i\}$   $i = 1$  to  $p$ .
- Calculate the energy  $J$  of the objective function by using the unconstrained abundances.
- Update the **best\_candidates\_list** through the negativity of the unconstrained abundances. The pixel with the most negative abundance is the best candidate, the pixel with the second most negative abundance is the second best candidate, ...

##### 3: Outer Loop ( $j$ keeps track of the $j$ th best candidate)

- Take  $r$  as best candidate currently: take the  $j$ th element of **best\_candidates\_list**.

##### 4: Inner Loop ( $i$ keeps track of the $i$ th endmember $e_i$ , $1 < i < p$ )

- Calculate the unconstrained abundances for  $\{e_1, e_2, \dots, e_{i-1}, r, e_{i+1}, \dots, e_p\}$  if this set of vector is linearly independent.
- Calculate the energy  $J_i$  of the objective function by using the unconstrained abundances.

##### 5: Replacement rule

- Once the algorithm exits from the Inner Loop, if any of the calculated energy ( $J_i$ ) of the objective function is lesser than the energy obtained by  $\{e_i\}$   $i = 1$  to  $p$  then
- The replacement is performed; therefore, the new set of endmembers is  $\{e_1, e_2, \dots, e_{i-1}, r, e_{i+1}, \dots, e_p\}$
- **counter** = **exhaustive\_counter**
- Update the **best\_candidates\_list** through the negativity of the unconstrained abundances. The pixel with most negative abundance is the best candidate, the pixel with the second most negative abundances is the second best candidate, ...
- Initialize  $j = 1$ .
- Go to Step 3.

##### 6: Exhaustivity counter decrementation

- **counter** is decremented by one.
- If counter does not reach 0, go to Step 3.

##### 7: Stopping rule

- Calculate the reconstructed image by multiplying the current set of endmembers in the original data space and its associated **unconstrained\_abundances** calculated in the original data space.
- If the reconstruction error power is lesser than the criterion exposed in Section II or  $p$  is equal to  $p_{end}$ , then go to Step 8.
- If not, increment  $p$  by one unit and update the end-members including  $e_p$ , as the best candidate (first element of **best\_candidates\_list**).
- Recalculate  $Y = U_{p-1}^T (X - \bar{X}) + \bar{X}$  with current  $p$ .
- Go to Step 2.

##### 8: Exit

- $A = E^+ X$ .

**OUTPUT:**  $E = [e_1, e_2, \dots, e_p]$ , **unconstrained Abundances A**

---

On the other hand, the second implementation, which is called NABO dimensional reduction (NABO\_DR), consists of projecting the data as  $Y' = U_{p-1}^T(X - \bar{X})$  and then constructing the  $Y$  matrix as  $[Y'; C]$ , with  $C = [c \ c \dots, \ c]$  being a  $1 \times N$  vector with  $c = \arg \max_{j=1\dots N} \| [X]_{:,j} \|$  as it is done by VCA in its preprocessing step. Thus, the algorithm works on a noiseless data set and with just  $p$  bands ( $p \ll L$ ), which increases the execution speed. Again, this projection has to be performed every time that variable  $p$  is increased. The pseudocode of this alternative implementation can be found in Algorithm 3.

---

### Algorithm 3 Pseudocode of NABO\_DR algorithm

---

**INPUTS:**  $p\_init$ ,  $p\_end$ , **exhaustivity\_counter**,  $X = [x_1, x_2, \dots, x_N]$ ;  
 $X$  is composed by  $N$  hyperspectral pixels

#### 1: Preprocessing

- Noise estimation for stopping rule.
- Obtaining  $U_{p\_end}$  by PCA.
- Initialize  $p$  to the **p\_init** value.
- $Z = U_{p-1}^T(X - \bar{X})$
- $C = [c \ c \ c \dots, \ c]$  with  $c = \arg \max_{j=1\dots N} \| [X]_{:,j} \|$
- $Y = [Z; C]$
- Let  $\{e_1, e_2, \dots, e_p\}$  be a set of initial vector randomly selected (or as input) from  $Y$ .

#### 2: Initialization

- Initialize **counter** to the **exhaustivity\_counter** value.
- Calculate the unconstrained abundances of every pixel of the image with the set of endmembers  $\{e_i\}$   $i = 1$  to  $p$ .
- Calculate the energy  $J$  of the objective function by using the unconstrained abundances.
- Update the **best\_candidates\_list** through the negativity of the unconstrained abundances. The pixel with the most negative abundance is the best candidate, the pixel with the second most negative abundance is the second best candidate, ...

#### 3: Outer Loop ( $j$ keeps track of the $j$ th best candidate)

- Take  $r$  as the best candidate currently: take the  $j$ th element of **best\_candidates\_list**.

#### 4: Inner Loop ( $i$ keeps track of the $i$ th endmember $e_i$ , $1 < i < p$ )

- Calculate the unconstrained abundances for  $\{e_1, e_2, \dots, e_{i-1}, r, e_{i+1}, \dots, e_p\}$  if this set of vector is linearly independent.
- Calculate the energy  $J_i$  of the objective function by using the unconstrained abundances.

#### 5: Replacement rule

- Once the algorithm exits from the Inner Loop, if any of the calculated energy ( $J_i$ ) of the objective function is lesser than the energy obtained by  $\{e_i\}$   $i = 1$  to  $p$  then
  - The replacement is performed; therefore, the new set of endmembers is  $\{e_1, e_2, \dots, e_{i-1}, r, e_{i+1}, \dots, e_p\}$
- **counter** = **exhaustive\_counter**
- Update the **best\_candidates\_list** through the negativity of the unconstrained abundances. The pixel with most negative abundance is the best candidate, the pixel with the second most negative abundances is the second best candidate, ...
- Initialize  $j = 1$ .
- Go to Step 3.

#### 6: Exhaustivity counter decrementation

- **counter** is decremented by one.
- If counter does not reach 0, go to Step 3.

#### 7: Stopping rule

- Calculate the reconstructed image by multiplying the current set of endmembers in the original data space and its associated unconstrained\_abundances calculated in the original data space.
- If the reconstruction error power is lesser than the criterion exposed in Section II or  $p$  is equal to **p\_end** then go to Step 8.
- If not, increment  $p$  by one unit and update the end-members including  $e_p$ , as the best candidate (first element of **best\_candidates\_list**).
- Recalculate  $Z = U_{p-1}^T(X - \bar{X})$  with current  $p$ .
- $Y = [Z; C]$
- Go to Step 2.

#### 8: Exit

- $E = U_{p-1} Z_{:,index} + \bar{X}$  {index is the vector with the endmembers index position in the image}.
- $A = E^+ X$ .

**OUTPUT:**  $E = [e_1, e_2, \dots, e_p]$ , **unconstrained Abundances A**

---

## IV. RESULTS

In this section, the unmixing performance of the three versions of the proposed NABO algorithm will be demonstrated and compared against different state-of-the-art solutions. For this purpose, we have used a set of artificially generated hyperspectral images and the real well-known *Cuprite* hyperspectral image collected by the Airborne Visible Infra-Red Imaging Spectrometer (AVIRIS). Furthermore, earlier, the endmember induction performance of the proposed NABO algorithm is compared against the one achieved by the method proposed in [30].

### A. Results With Synthetic Hyperspectral Images

The artificial hyperspectral images used in this paper were generated with the demo\_vca software tool available from [5], which allows creating a hyperspectral image of a spatial size

defined by the user from  $p$  spectral signatures selected from the U.S. Geological Survey digital spectral library<sup>1</sup> that are mixed according to abundance fractions generated with a properly tuned Dirichlet distribution. To include the illumination variability that typically occurs in real scenes, we have introduced in the process of generating these images a variable named *fluct* that measures the variance of this illumination variability. Hence, each pixel of the image, which is obtained by multiplying the actual endmembers and the actual abundances, is further multiplied by a positive factor that follows the distribution  $\mathcal{N}(1, \sigma^2)$ , where  $\sigma^2 = \text{fluct}$ . In addition, a certain amount of Gaussian white noise is added at the end of this image generation process, so that the SNR of the created images can be fixed to a certain predefined value.

Figs. 2–5 show the results obtained for a set of synthetically generated hyperspectral images composed by  $150 \times 150$  pixels and 224 spectral bands with four different numbers of endmembers (5, 10, 15, and 20), four different SNR values (10, 20, 30, and 40 dBs), and under two different scenarios with respect to the lack or presence of illumination variability in the scene (*fluct* = 0 and *fluct* =  $3e-2$ , respectively). Each of the three versions of the proposed NABO algorithm (NABO, NABO\_NN, and NABO\_DR) has been applied to these images considering the values 1 and 5 for the **exhaustivity\_counter** variable (see the pseudocodes shown at Algorithms 1–3) to study the influence of the degree of exhaustiveness within the search process over the global performance of the proposed algorithm. Moreover, each version of the algorithm has been applied to each image a total of ten times, considering at each run a different and randomly selected seed, i.e., a set of starting points for the search process. To make a fair comparison, in Figs. 2–5, the abundances obtained by the proposed NABO algorithms, the VCA [5], and N-FINDR [9] algorithms have been estimated using a fully constrained abundance estimator (fully constrained least squares, FCLS) [25]. The unconstrained abundances obtained by the different versions of the NABO algorithm are not used in the comparisons. This comparison has been done in terms of the average spectral angle (SA) [2] between the real and the extracted endmembers (see Fig. 2), the abundance RMSE (see Fig. 3), the abundance signal-to-reconstruction error (SRE) measured in decibels as defined in [18] (see Fig. 4), and the execution time (see Fig. 5), which has also been reported as an important metric in SU [27]–[29]. At this point, it is important to mention that, for all these cases, the real number of endmembers have been signaled as an input for all the algorithms, whereas the abundances have been forced to be fully constrained. This means that, in all the simulations, the value of **p\_init** has been preset to 3 and the value of **p\_end** has been preset to the value of the actual number of endmembers present in the scene for the three versions of the proposed NABO algorithm.

From these four figures, the following conclusions can be extracted.

- 1) Due to their corresponding preprocessing stages, NABO\_NN and NABO\_DR exhibit much better

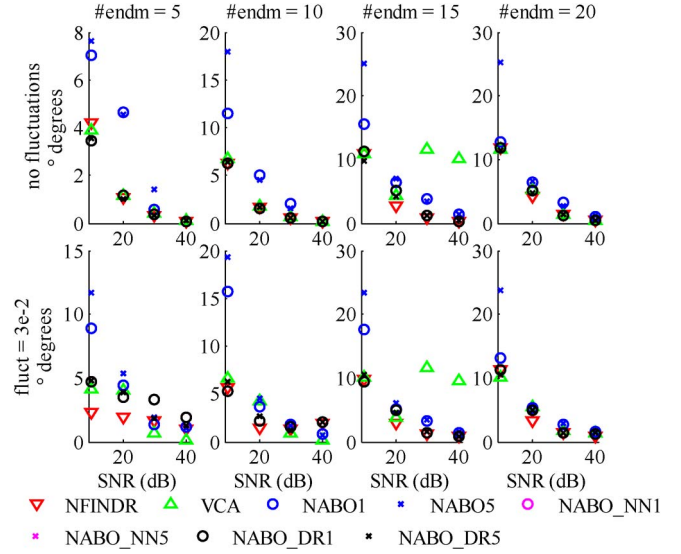


Fig. 2. Mean SA for synthetic hyperspectral images of a spatial size of  $150 \times 150$  pixels (known  $p$ ). The results obtained by the NABO\_NN algorithm are hidden by the results obtained by the NABO\_DR algorithm since both results are the same.

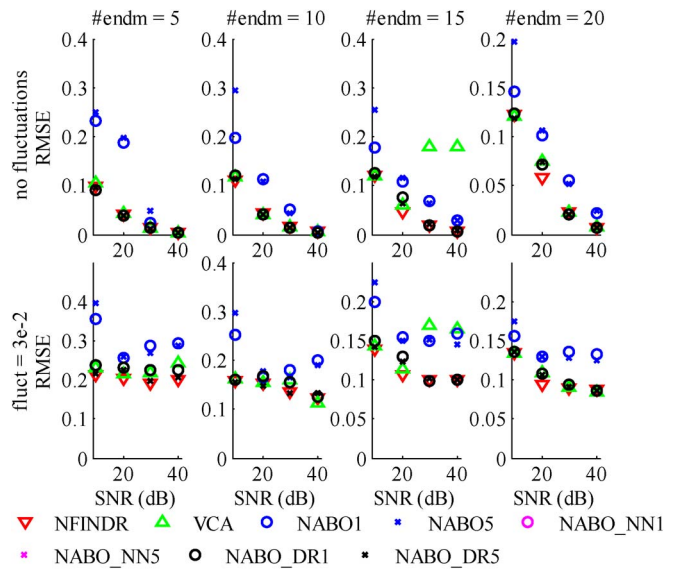


Fig. 3. Mean abundance RMSE for synthetic hyperspectral images of a spatial size of  $150 \times 150$  pixels (known  $p$ ). The results obtained by the NABO\_NN algorithm are hidden by the results obtained by the NABO\_DR algorithm since both results are the same.

- performance than the NABO algorithm in terms of the accuracy of the extracted endmembers (SA), and the quality of the abundances (RMSE and SRE), with independence of the number of endmembers, the noise, and/or the illumination fluctuations (spectral variability) present in the hyperspectral scene. Moreover, it is worth to mention that, for all the cases, NABO\_NN and NABO\_DR were able to compute exactly the same endmembers and abundances given the fact that they used the same seed in each case.
- 2) The three proposed algorithms do not generally benefit from a higher degree of exhaustiveness within their internal search processes, in the sense that fixing the

<sup>1</sup><http://speclab.cr.usgs.gov>

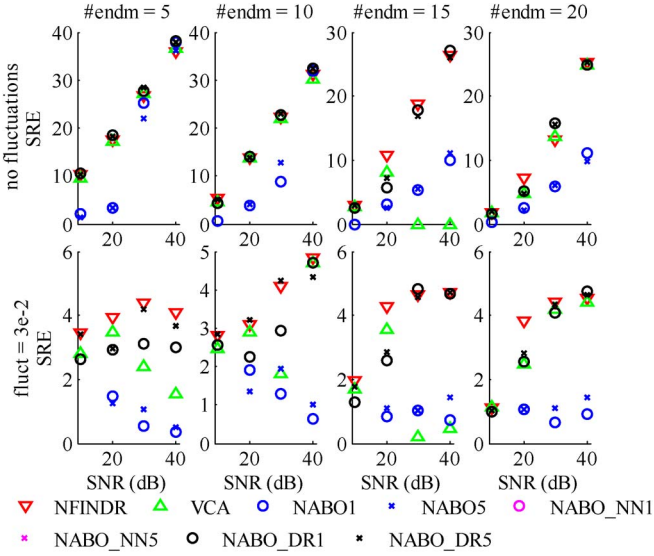


Fig. 4. Mean abundance SRE for synthetic hyperspectral images of a spatial size of  $150 \times 150$  pixels (known  $p$ ). The results obtained by the NABO\_NN algorithm are hidden by the results obtained by the NABO\_DR algorithm since both results are the same.

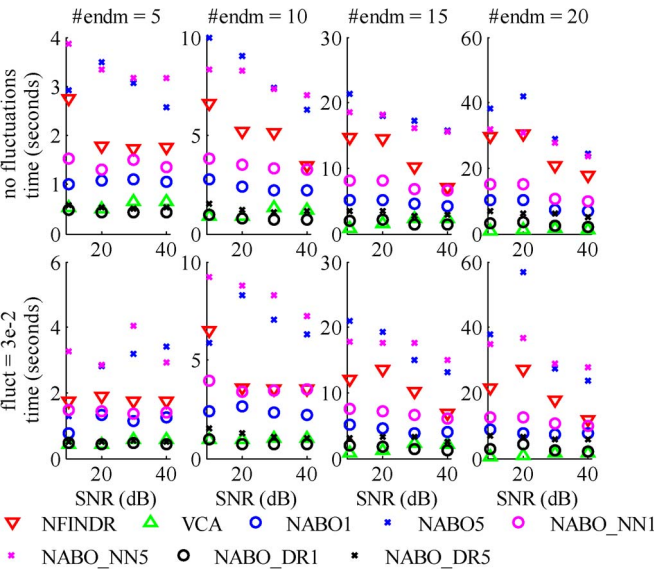


Fig. 5. Mean execution time for synthetic hyperspectral images with a spatial size of  $150 \times 150$  pixels (known  $p$ ).

value of the **exhaustivity\_counter** to 5 does not imply always the achievement of more accurate endmembers and abundances with respect to the situation in which the value of this counter is set to 1. Furthermore, this increase in the exhaustiveness of the search process brings an increase in the computational cost demanded by each algorithm. In any case, it is worth to mention that this extra computational effort is much more noticeable in the NABO and NABO\_NN algorithms than in the NABO\_DR algorithm, where in fact the differences between the time required by the NABO\_DR1 and the NABO\_DR5 algorithms (see Fig. 5) are almost negligible. Given this fact, we can consider the algorithm results highly independent of the exhaustiveness although, as shown in Section IV-C,

increasing the exhaustivity increases the robustness of the algorithm against outlier pixels. Furthermore, we consider the algorithm highly independent of the parameters **p\_init** and **p\_end** as well since the parameters **p\_init** and **p\_end** can also be set to high conservative values that does not affect the final result and since these parameters are considered part of the implementation and not part of the algorithm itself. The two main reasons why the authors have not discarded them are: 1) setting **p\_init** to a conservative low value makes the proposed method less sensitive to the random seed since the algorithm has more flexibility to converge to the actual endmembers; and 2) if the user knows the actual number of endmembers, the user can set **p\_end** to the actual number of endmembers and force the algorithm to reach that number instead of checking the condition exposed in Section II-A.

- 3) The endmembers and the abundances obtained by the proposed NABO\_DR algorithm (and consequently by the NABO\_NN algorithm) are very similar to the ones obtained by the N-FINDR case (see Figs. 2–4), whereas NABO\_DR exhibits a much lower computational cost (see Fig. 5).
- 4) The endmembers and the abundances obtained by the proposed NABO\_DR algorithm (and consequently by the NABO\_NN algorithm) are generally better than the ones obtained by the VCA case (see Figs. 2–4), although both approaches exhibit a similar computational cost (see Fig. 5).

Furthermore, to study the influence of the spatial size of the image under processing over the performance achieved by our algorithms, we have run the same simulations but with images of a spatial size of  $250 \times 250$  pixels. The results, which are shown in Figs. 6–9, demonstrate that the performance achieved by our algorithms does not depend of the spatial dimensions of the image under processing, in the sense that the same four conclusions as before can be extracted from the analysis of the data displayed in Figs. 6–9.

At this point, we note a strange behavior of the VCA algorithm for this data set when the noise decreases and when the number of endmembers is set to 15. The VCA is a data-dependent algorithm, and in this particular experiment, it underperformed with regard to other algorithms, although the algorithm is generally very competitive (as it can be seen in other experiments reported in this paper with the VCA). The results reported correspond to an average of 10 VCA runs so we feel that this result cannot be explained by an occasional bad run of the algorithm.

Once the ability of the three proposed algorithms for accurately extracting endmembers has been proved, we have performed a new set of simulations to validate the goodness of our proposals for fully unmixing a given hyperspectral image, i.e., estimate its number of endmembers, extract them from the image, and obtain their respective abundance fractions. In this sense, Figs. 10–12 show the results obtained by the three versions of the NABO algorithm when fully unmixing hyperspectral images composed by  $250 \times 250$  pixels and 224 spectral bands in terms of the estimated number of endmembers

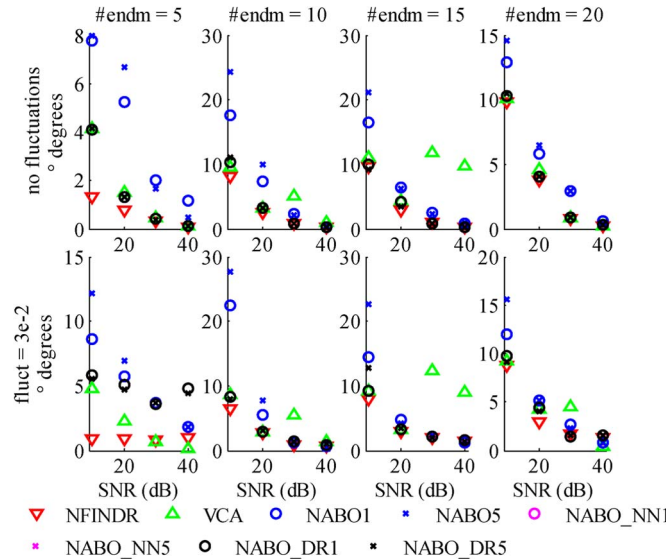


Fig. 6. Mean SA for synthetic hyperspectral images of a spatial size of  $250 \times 250$  pixels (known  $p$ ). The results obtained by the NABO\_NN algorithm are hidden by the results obtained by the NABO\_DR algorithm since both results are the same.

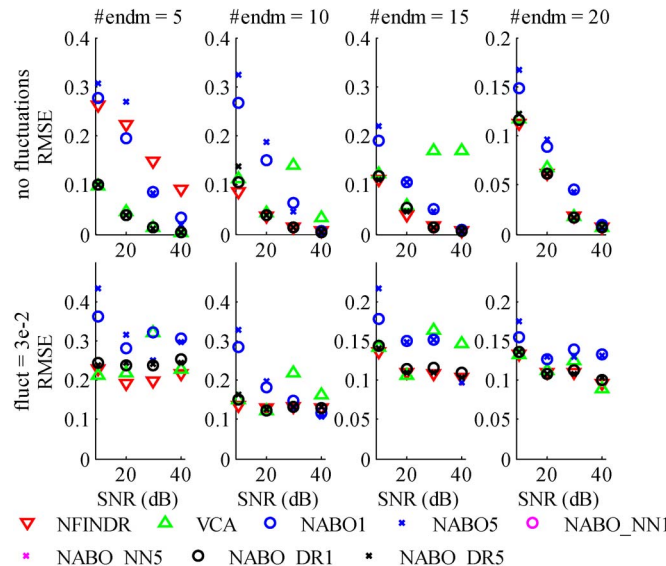


Fig. 7. Mean abundance RMSE for synthetic hyperspectral images of a spatial size of  $250 \times 250$  pixels (known  $p$ ). The results obtained by the NABO\_NN algorithm are hidden by the results obtained by the NABO\_DR algorithm since both results are the same.

(see Figs. 10 and 11) and the achieved RMSE (see Fig. 11) when reconstructing the image. For all the simulations, the value of  $\mathbf{p}_{\text{init}}$  has been fixed to 3, whereas for the value of  $\mathbf{p}_{\text{end}}$ , it has been established as an overestimated value equal to the actual number of endmembers plus 20 units. The results in Figs. 10 and 11 have been compared with the ones obtained with the state-of-the-art VD (more concretely, the VD was estimated by the NWHFC eigentresholding method [20] using the Neyman–Pearson test with the false-alarm probability set to  $10^{-3}$ ,  $10^{-4}$ , and  $10^{-5}$ , although we only present the estimations for false alarm set to  $10^{-4}$  since the differences between them are negligible) and HySime [22], whereas the results shown in Fig. 12 have been again compared with the

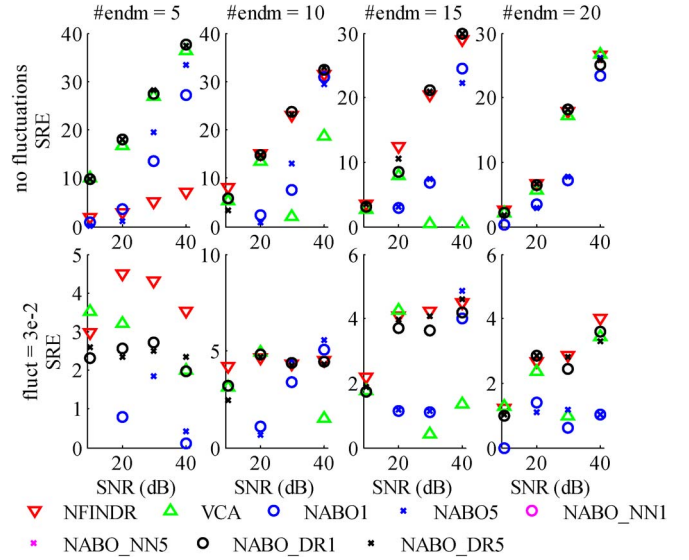


Fig. 8. Mean abundance SRE for synthetic hyperspectral images of a spatial size of  $250 \times 250$  pixels (known  $p$ ). The results obtained by the NABO\_NN algorithm are hidden by the results obtained by the NABO\_DR algorithm since both results are the same.

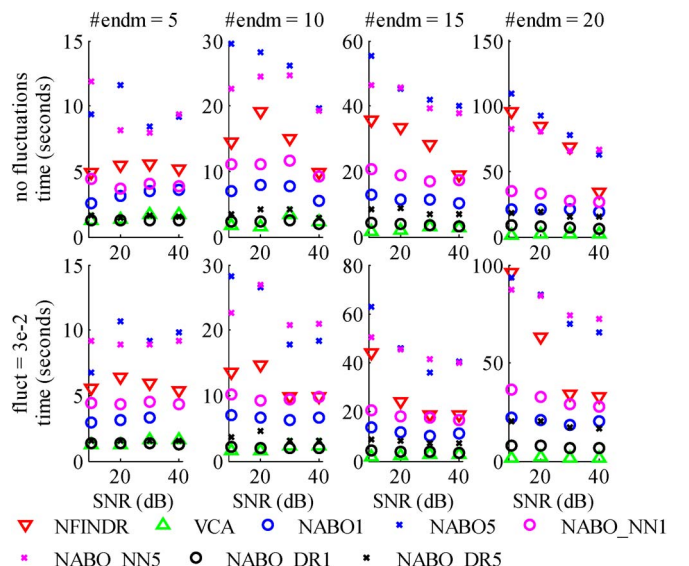


Fig. 9. Mean execution time for synthetic hyperspectral images of a spatial size of  $250 \times 250$  pixels (known  $p$ ).

ones provided by the N-FINDR and the VCA algorithms when both are preceded by the HySime algorithm and succeeded by a fully constrained estimation of the abundances. At this point, it is worth to mention that we have not provided comparisons in terms of average spectral angles and abundance SREs as we did in previous simulations to avoid inconsistencies derived from the fact that the number of endmembers obtained by the HySime algorithm may differ from the ones obtained by the different versions of the NABO algorithm.

The results shown in Figs. 10 and 11 reveal that, when dealing with images with SNR of 40 dBs or above, all the NABO versions are able to provide very good estimates of the number of endmembers that constitute the hyperspectral image under analysis. However, when the SNR goes below

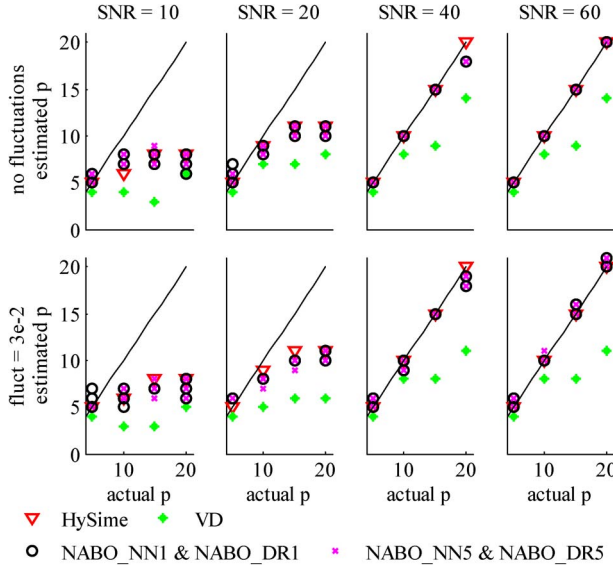


Fig. 10. Estimation of the number of endmembers for synthetic hyperspectral images of a spatial size of  $250 \times 250$  pixels. Algorithms HySime, VD, NABO\_NN, and NABO\_DR. NABO\_NN and NABO\_DR methods were applied to each image a total of ten times, considering at each run a different and randomly selected seed. NABO\_NN and NABO\_DR obtained exactly the same results.

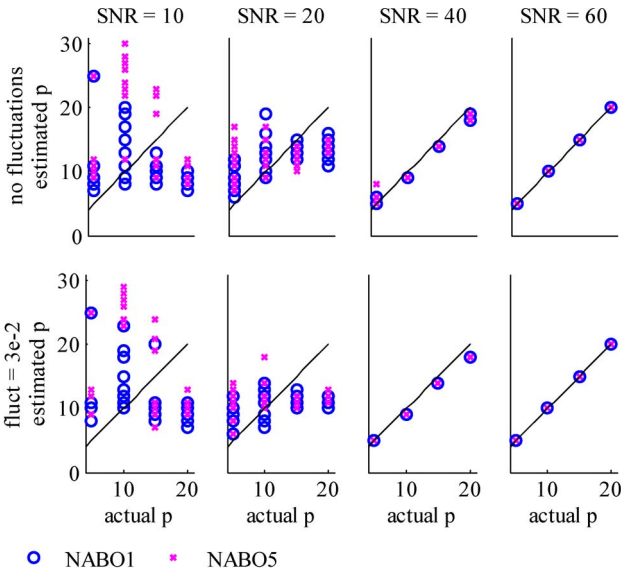


Fig. 11. Estimation of the number of endmembers for synthetic hyperspectral images of a spatial size of  $250 \times 250$  pixels for algorithm NABO. The method was applied to each image a total of ten times, considering at each run a different and randomly selected seed.

40 dBs, the original NABO algorithm provides different and variable results when compared with the NABO\_NN and the NABO\_DR algorithms which, again, are able to provide exactly the same results in all the cases. In any case, it is important to highlight that the NABO\_DR algorithm (and subsequently the NABO\_NN algorithm) always provides much better estimates than the VD algorithm and very similar estimates than the ones provided by the HySime algorithm. It is important to notice that the noise estimator used by the three different implementations of NABO is the same estimator used by HySime, which could explain these similarities. In addition, Fig. 12 demonstrates that the NABO\_DR algorithm obtains lower RMSE values when

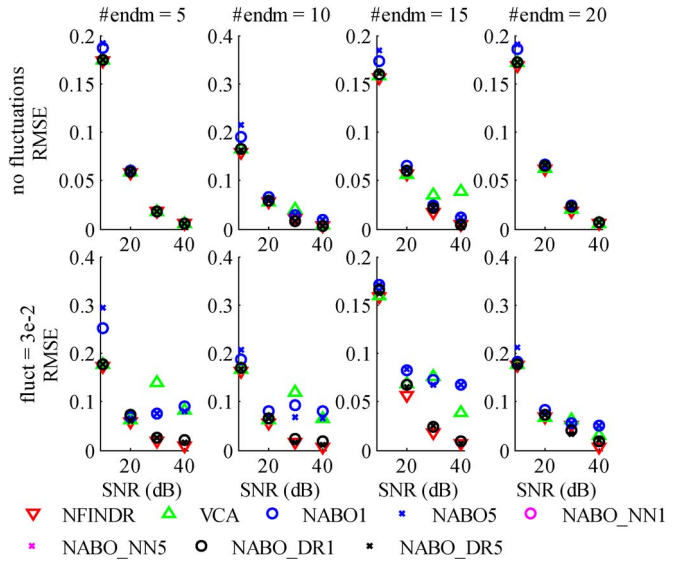


Fig. 12. Mean reconstruction RMSE for synthetic hyperspectral images of a spatial size of  $250 \times 250$  pixels. The results obtained by the NABO\_NN algorithm are hidden by the results obtained by the NABO\_DR algorithm since both results are the same.

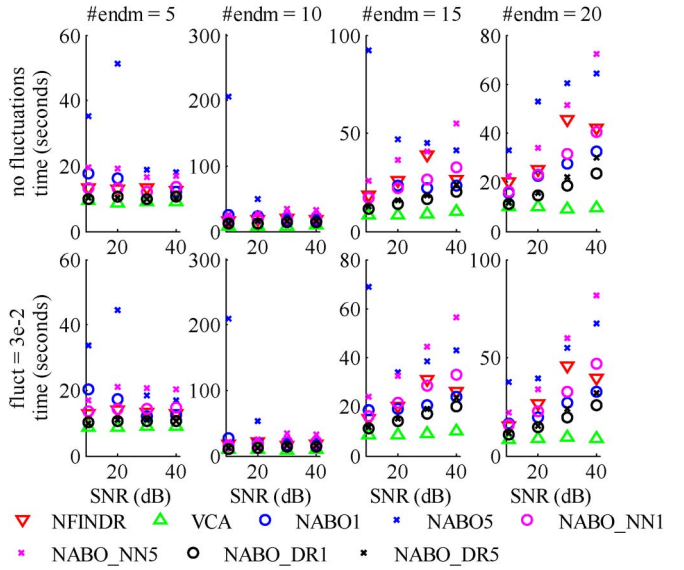


Fig. 13. Mean execution time for synthetic hyperspectral images of a spatial size of  $250 \times 250$  pixels.

compared with a fully constrained hyperspectral unmixing chain composed by the HySime and VCA algorithms and very similar values than the ones achieved with the same processing chain but replacing the VCA by the N-FINDR algorithm. Last but not the least, it is important to highlight that the unmixing procedure carried out by the NABO\_DR algorithm is much faster than the one based on the use of the HySime and N-FINDR algorithms, as demonstrated in Fig. 13. At this point, it is also fair to mention that the combination of HySime and VCA algorithms demands a lower computational effort than the proposed NABO\_DR algorithm.

#### B. Results With Real Hyperspectral Images

The well-known Cuprite mineralogical scene, which has been widely used to validate the accuracy of hyperspectral



Fig. 14. False color combination of the *Cuprite* scene used in experiments.

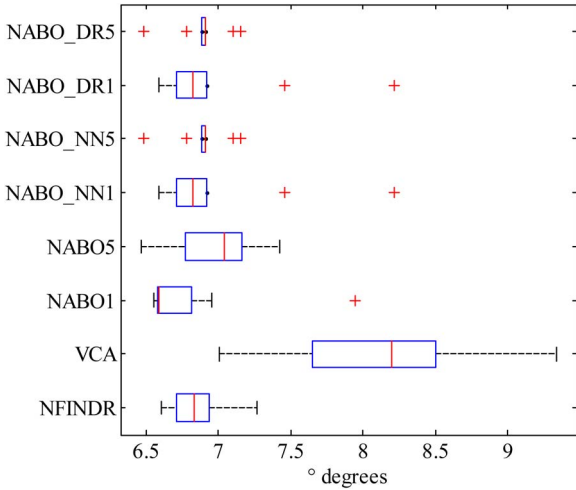


Fig. 15. Mean SA for the *Cuprite* scene with  $p = 14$ .

unmixing algorithms, has been also taken into account in this paper. This scene was captured by NASA's AVIRIS sensor over the Cuprite mining district in Nevada. Concretely, we have used a  $250 \times 191$ -pixel subset available online<sup>2</sup> in reflectance units after atmospheric correction which comprises 224 spectral bands between 0.4 and  $2.5 \mu\text{m}$ . Prior to the analysis, different bands have been removed due to water absorption and low SNR, leaving a total of 192 reflectance channels to be used in our tests. For illustrative purposes, Fig. 14 shows a false color combination of the hyperspectral data set used in our experiments.

Figs. 15–17 show the results obtained for the aforementioned *Cuprite* scene when the number of endmembers is preset for all the versions of the NABO algorithm. In particular, we have set the total number of endmembers to  $p = 14$  as it is the most common value found in the state-of-the-art for this particular portion of the *Cuprite* scene [5]. The results obtained in terms of the average spectral angle scores obtained after comparing

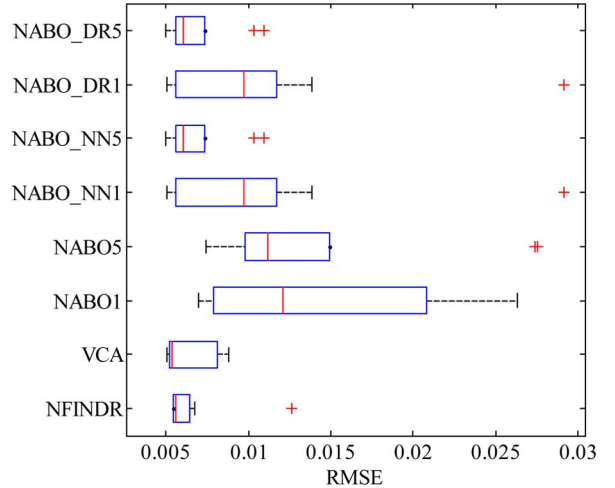


Fig. 16. Mean reconstruction RMSE for the *Cuprite* scene with  $p = 14$ .

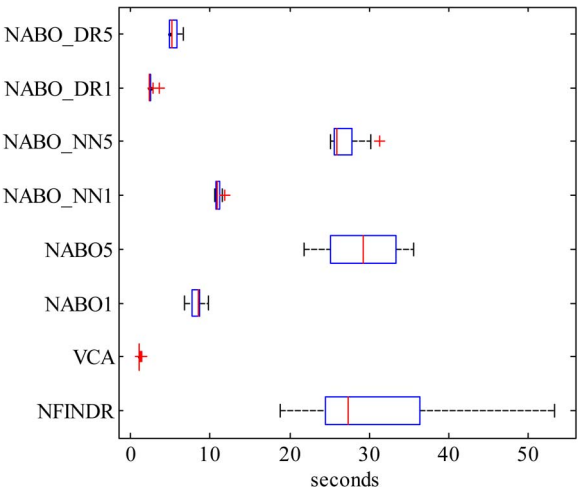


Fig. 17. Mean execution time for the *Cuprite* scene with  $p = 14$ .

the USGS library spectra of alunite, buddingtonite, calcite, kaolinite, and muscovite with the corresponding endmembers extracted by the different algorithms from the *Cuprite* scene (see Fig. 15), the average RMSE obtained after performing the reconstruction of the image (see Fig. 16), and the execution time to unmix the targeted *Cuprite* sub-image (see Fig. 17), have been represented in the form of boxplots. Since each algorithm was run several times, boxplots are a convenient way to present the different results achieved. In these plots, blue boxes represent the range between the first quartile Q1 and the third quartile Q3, whereas the red line inside the box represents the median. Moreover, the interquartile range IQR is defined as the first quartile subtracted from the third quartile, i.e.,  $\text{IQR} = Q3 - Q1$ . Thus, every result that falls outside the range  $[Q1 - 1.5 \cdot \text{IQR}, Q3 + 1.5 \cdot \text{IQR}]$  is considered an outlier, and it is represented as a red cross, whereas the maximum and minimum results that fall inside the mentioned range are represented by the so-called whiskers, i.e., the lines extending horizontally from the blue boxes. For illustrative purposes, the error maps obtained after reconstructing the original hyperspectral image using the endmembers provided by different algorithms using  $p = 14$  (in one specific run of the multiple ones that

<sup>2</sup><http://aviris.jpl.nasa.gov/free-data>

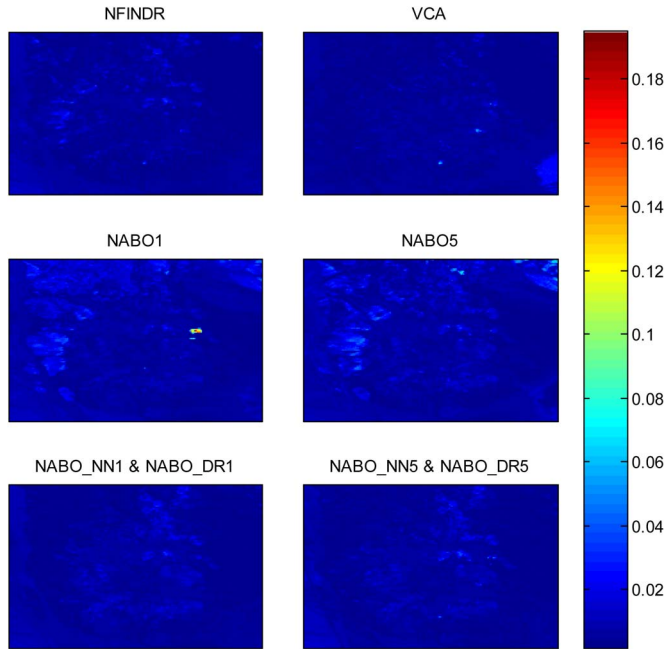


Fig. 18. Error maps obtained after reconstructing the *Cuprite* scene with  $p = 14$  using the endmembers provided by different algorithms.

were conducted by each algorithm) are provided in Fig. 18 for clarity. These results demonstrate that, in particular, the proposed NABO\_DR algorithm represents a feasible solution for unmixing a given hyperspectral image, in the sense that it provides an unmixing performance similar to the solution based on the use of the N-FINDR algorithm (see Figs. 15 and 16) but with a computational cost equivalent to a processing chain based on the utilization of the VCA algorithm (see Fig. 17).

Moreover, we have also tested our algorithms in the situation where the number of endmembers is unknown *a priori*. In this sense, Fig. 19 shows that, when the different versions of the proposed NABO algorithm are applied to the Cuprite data set with  $p_{\text{init}} = 3$  and  $p_{\text{end}} = 25$ , the median of the number of endmembers obtained lies always between 13 and 15 endmembers, which is in agreement with the most commonly accepted value for this scene, which is 14 endmembers. Furthermore, when the results provided by the NABO\_DR algorithm are compared with the ones provided by the N-FINDR and the VCA algorithms when both are preceded by the HySime algorithm and succeeded by a fully constrained estimation of the abundances, we come again to the conclusion that this particular version of the proposed algorithm represents an excellent tradeoff solution in terms of unmixing performance versus computational cost when compared with these state-of-the-art approaches, as the data shown in Figs. 20–22 reveals. At this point, it is important to highlight that the average SAs and RMSEs obtained by the N-FINDR-based and the VCA-based unmixing solutions have been obtained assuming that the number of endmembers in the scene equals to 18, which is the result given by the HySime algorithm. Hence, these two solutions have bigger chances to extract from the image endmembers more similar to the five pure signatures already mentioned (alunite, buddingtonite, calcite, kaolinite, and muscovite) as well as to obtain much better reconstructed images, which play against

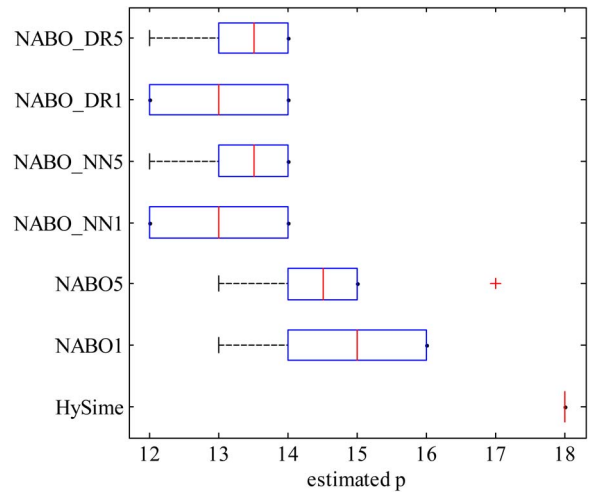


Fig. 19. Estimation of the number of endmembers for the *Cuprite* scene.

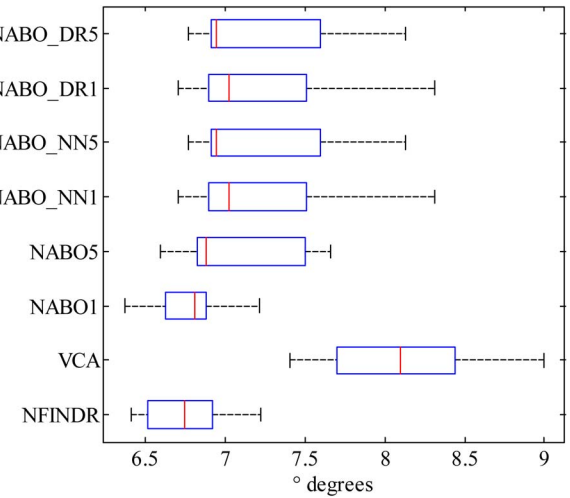


Fig. 20. Mean SA for the *Cuprite* scene. Results obtained by NABO\_NN1 and NABO\_NN5 are the same than NABO\_DR1 and NABO\_DR5, respectively. The number of endmembers for VCA and NFINDR is  $p = 18$  (HySime). The different NABO versions estimate the number of endmembers in the range  $p = [12, 16]$ .

our proposals. Nonetheless, and even under this unfavorable scenario, the NABO\_DR algorithm (particularly in its more exhaustive version) is able to achieve very competitive levels in terms of endmember extraction accuracy and reconstruction ability as it is demonstrated in the scatter plot shown in Fig. 23.

### C. Comparison of the Proposed NABO Method Against Xu *et al.*'s Method [30]

Here, we present the comparison between NABO\_DR with different values for the **exhaustivity\_counter** and our implementation of the method proposed in [30] with different tolerances. In this comparison, we want to illustrate that NABO has low sensitivity to outliers, highlighting the relevance of the proposed NABO global objective function. We would like to remark that the method proposed in [30] allows the use of spatial information to address the presence of outliers. However, injecting spatial information in [30] would mask our purpose.

The comparison is made using artificial hyperspectral images with and without outliers. The artificial hyperspectral images

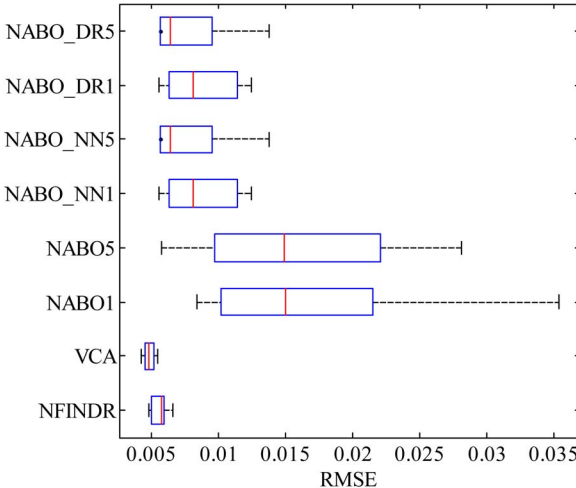


Fig. 21. Mean reconstruction RMSE for the *Cuprite* scene. Results obtained by NABO\_NN1 and NABO\_NN5 are the same than NABO\_DR1 and NABO\_DR5, respectively. The number of endmembers for VCA and NFINDR is  $p = 18$  (HySime). The different NABO versions estimate the number of endmembers in the range  $p = [12, 16]$ .

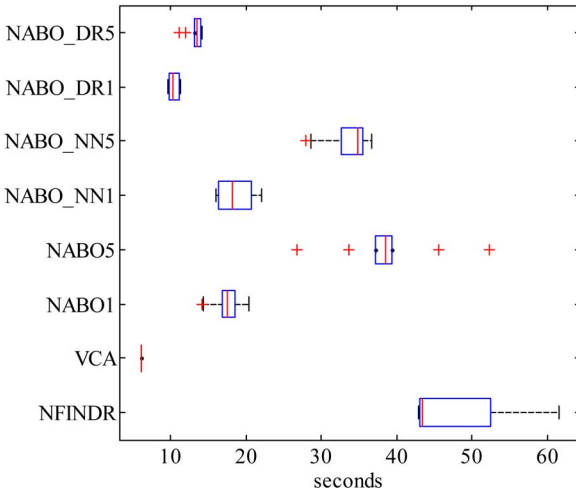


Fig. 22. Mean execution time for the *Cuprite* scene. The number of endmembers for VCA and NFINDR is  $p = 18$  (HySime). The different NABO versions estimate the number of endmembers in the range  $p = [12, 16]$ .

were generated with the *demo\_vca* software tool available from [5]. We generate 50 different images of  $150 \times 150$  pixels size and 224 spectral bands, considering ten endmembers and a SNR of 30 dBs without illumination fluctuations (spectral variability). In the experiment with outliers, we introduced 200 outliers (0.89% of the total number of pixels). These outliers consist of random vectors obtained from a uniform distribution in the range  $[0, 0.5]$ . In all the cases, we considered that the number of endmembers searched by the algorithms is known *a priori* since [30] does not estimate the number of endmembers, i.e., in these experiments, NABO\_DR is not estimating the number of endmembers. Furthermore, all the methods used a different random seed for all the images. The **exhaustivity\_counter** values for NABO\_DR algorithm are set to 1, 5, 20, and 100, and the tolerances for [30] are set to 0.01 and 0.001.

Figs. 24–26 show the results obtained for the case without outliers. In Fig. 24, we show the average SA between the induced endmembers and the true ones. All the methods

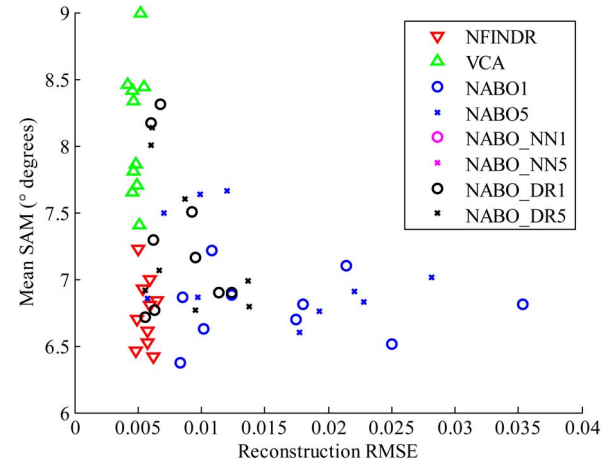


Fig. 23. Scatter plot: RMSE versus SA for the *Cuprite* scene. Results obtained by NABO\_NN1 and NABO\_NN5 are the same than NABO\_DR1 and NABO\_DR5, respectively. The number of endmembers for VCA and NFINDR is  $p = 18$  (HySime). The different NABO versions estimate the number of endmembers in the range  $p = [12, 16]$ .

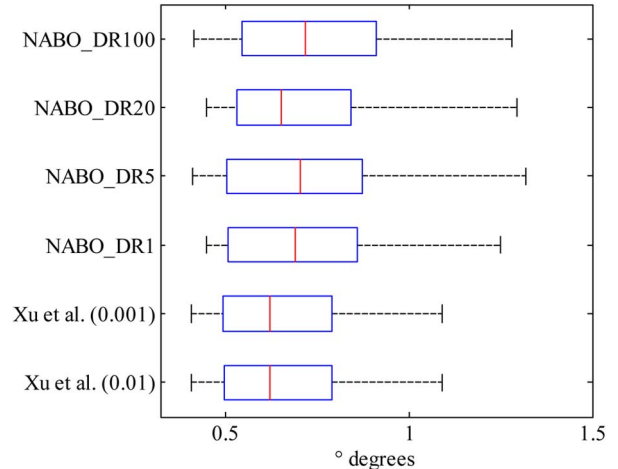


Fig. 24. Mean SA for synthetic hyperspectral images of a spatial size of  $150 \times 150$  pixels, known  $p = 10$ , SNR = 30 dBs without outliers.

obtained similar results, although the results obtained in [30] with both tolerances are slightly better. However, in Fig. 25, we show that the RMSE of the FCLS abundances is lower for the proposed methods in comparison with our implementation of [30] when no spatial information is taken into account. In general, the higher the exhaustiveness of the proposed method, the lower the RMSE. Regarding the execution time, in Fig. 26, we show the time needed by the different methods. The method in [30] exhibits the fastest executions, independently of the tolerance value, although the differences with NABO\_DR1 and NABO\_DR5 are negligible. As expected, for the NABO\_DR methods, the higher the **exhaustivity\_counter**, the higher the execution time.

Figs. 27–29 show the results obtained for the case with outliers. In Fig. 27, we show the average SA between the induced endmembers and the true ones. In this case, the NABO\_DR method exhibits better results than the ones in [30]. The same trend is shown in Fig. 28 for the abundance RMSE. Hence, it is worth noting that NABO\_DR is more robust against outliers than the method in [30] when spatial information is not injected.

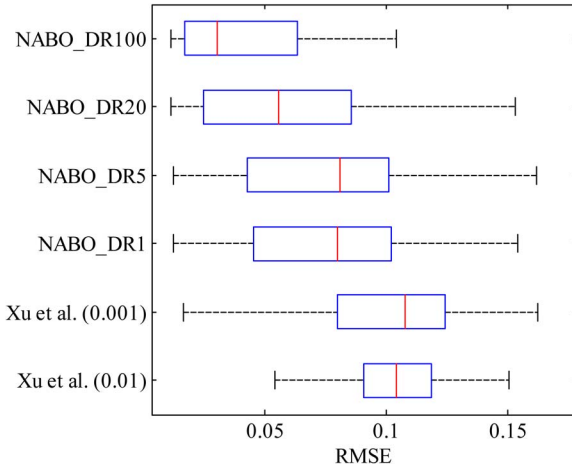


Fig. 25. Mean abundance RMSE for synthetic hyperspectral images of a spatial size of  $150 \times 150$  pixels, known  $p = 10$ , SNR = 30 dB without outliers.

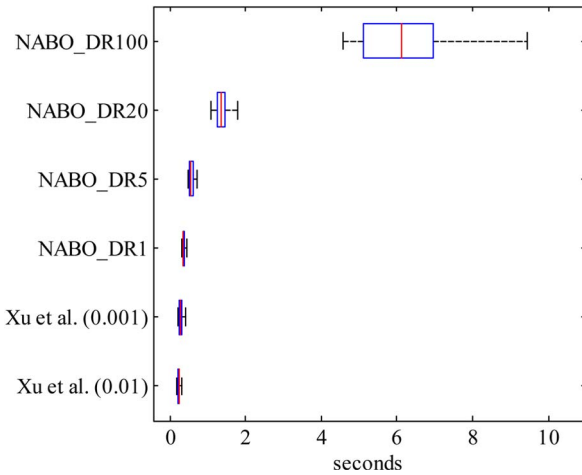


Fig. 26. Execution time for synthetic hyperspectral images of a spatial size of  $150 \times 150$  pixels, known  $p = 10$ , SNR = 30 dBs without outliers.

In this case, the higher the **exhaustivity\_counter**, the higher the robustness to outliers. This demonstrates the utility of this parameter and the validity of the global objective function.

Finally, Fig. 29 shows a similar execution time trend than the one reported for the case without outliers, except for the fact that the execution times are lower. Hence, the higher the **exhaustivity\_counter**, the higher the robustness of the algorithm, at the cost of increasing computational time.

## V. DISCUSSION

Up to this point, we have studied the algorithmic aspects of NABO, showing how the different algorithm variants behave in terms of the different parameters, i.e., **p\_init**, **p\_end**, and **exhaustivity\_counter**. In the following, we provide guidelines on the implementation aspects of the different NABO variants. First of all, given the results shown in Section IV, NABO\_DR is the best algorithm variant from all viewpoints since it exhibits the best performance in terms of the accuracy of the extracted endmembers and the quality of the abundances and its associated computational cost. However, the implementation complexity of NABO\_DR is higher than the implementation of

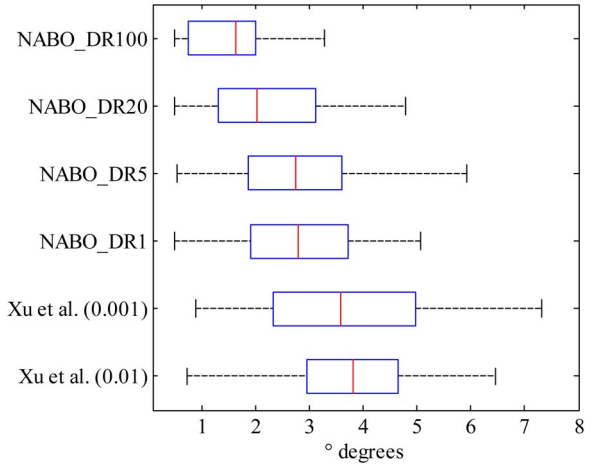


Fig. 27. Mean SA for synthetic hyperspectral images of a spatial size of  $150 \times 150$  pixels, known  $p = 10$ , SNR = 30 dBs with outliers (0.89% of the total number of pixels).

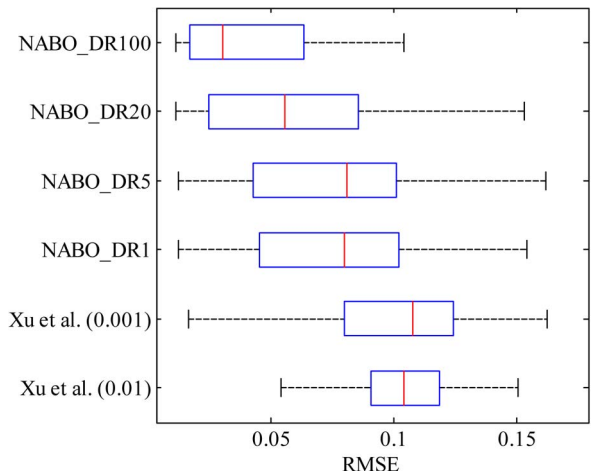


Fig. 28. Mean abundance RMSE for synthetic hyperspectral images of a spatial size of  $150 \times 150$  pixels, known  $p = 10$ , SNR = 30 dBs with outliers (0.89% of the total number of pixels).

NABO due to the need of NABO\_DR to extract the principal components of the image and the need to redefine the image in terms of these principal components every time the number of endmembers is increased.

Second, we further describe some aspects to bear in mind when setting the different parameters. Regarding **p\_init**, we recommend to set it to a low value, i.e.,  $p\_init = 3$ . A low value makes the method less sensitive to the random seed since the method will have more flexibility to exchange the considered endmembers in the first steps. With respect to **p\_end**, if the number of endmembers in the image is known, **p\_end** should be set to the actual number of endmembers, forcing the algorithm to reach that number instead of checking the condition exposed in Section II-A. Otherwise, we recommend using a conservative value since the algorithm eventually stops close to the actual number of endmembers. However, **p\_end** defines the number of principal components extracted in the preprocessing; therefore, a value that is set too high could have some impact in computational cost and in the amount of memory required depending on

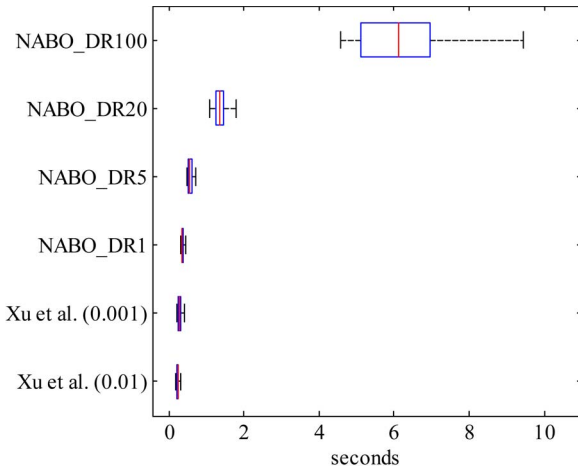


Fig. 29. Execution time for synthetic hyperspectral images of a spatial size of  $150 \times 150$  pixels, known  $p = 10$ , SNR = 30 dBs dBs with outliers (0.89% of the total number of pixels).

the platform in which is implemented. Finally, regarding **exhaustivity\_counter**, we have shown that the higher the **exhaustivity\_counter**, the higher the robustness of the method, particularly when dealing with outliers. Nevertheless, increasing the exhaustiveness of the search process brings an increase in the computational cost demanded by the method. Hence, we recommend setting this value to one by default (optimal computational cost). However, in some cases, it is worth increasing this value. For instance, when there are outliers in the image, increasing the **exhaustivity\_counter** improves the robustness of the NABO algorithm. Moreover, when handling small sized images, the benefit of the robustness given by a higher value of the **exhaustivity\_counter** could overcome the impact in the computational cost, which depends on the size of the image.

## VI. CONCLUSION AND FUTURE LINES OF RESEARCH

In this paper, we have developed a new NABO algorithm for SU of hyperspectral scenes under the LMM assumption. The algorithm assumes the presence of pure pixels in the scene and provides solutions that are competitive with regards to those offered by other state-of-the-art algorithms in terms of both unmixing accuracy and computational performance. One of the main features of the algorithm is that it provides a full SU chain covering the three main steps involved in hyperspectral unmixing. First, it provides a simple mechanism for estimating the number of endmembers in the scene, which is also feasible for other algorithms. This mechanism is highly effective and reliable for estimating the number of endmembers. Then, it uses the negative abundances obtained in abundance estimation as a criterion to identify the endmember signatures with high precision, thus providing not only the endmember signatures but also their abundances, as opposed to many other algorithms, which are more specific. The algorithm can also be easily adapted to a scenario in which the number of endmembers is known in advance, and two additional variations of the algorithm have been presented to deal with high-noise scenarios and to significantly reduce its execution time.

As with any new approach, there are still some unresolved issues that may present challenges over time. For instance, the noise estimation part can be further developed since it is an important issue regarding the quality of the estimation of the number of endmembers. Some ideas have already emerged, such as estimating the noise from the unused components of the PCA preprocessing which would be consistent with the algorithm if feasible. In addition, the energy objective function that the algorithm minimizes is currently based on spectral information alone, although the inclusion of spatial information could provide additional advantages in future developments of the method. The adaptation of the method to scenarios without the pure pixel assumption is also a relevant future direction, as well as the development of additional comparisons with SU algorithms, particularly those under the minimum volume and sparse regression regimes. Although our algorithm represents, to the best of our knowledge, the first solution that covers the three main steps in SU, additional comparisons of each of these steps to other methods should also be conducted in future developments.

## ACKNOWLEDGMENT

The authors would like to thank the Associate Editor and the Anonymous Reviewers for their very interesting comments and suggestions, which greatly helped us to improve the technical quality and presentation of our manuscript.

## REFERENCES

- [1] J. M. Bioucas-Dias *et al.*, "Hyperspectral unmixing overview: Geometrical, statistical and sparse regression-based approaches," *IEEE J. Sel. Topics Appl. Earth Observ. Remote Sens.*, vol. 5, no. 2, pp. 354–379, Apr. 2012.
- [2] N. Keshava and J. Mustard, "Spectral unmixing," *IEEE Signal Process. Mag.*, vol. 19, no. 1, pp. 44–57, Jan. 2002.
- [3] A. Plaza, G. Martin, J. Plaza, M. Zortea, and S. Sánchez, "Recent developments in spectral unmixing and endmember extraction," in *Optical Remote Sensing*, S. Prasad, L. M. Bruce, and J. Chanussot, Eds. Berlin, Germany: Springer-Verlag, 2011, ch. 12, pp. 235–267.
- [4] C.-I. Chang and D. Heinz, "Constrained subpixel target detection for remotely sensed imagery," *IEEE Trans. Geosci. Remote Sens.*, vol. 38, no. 3, pp. 1144–1159, May 2000.
- [5] J. Nascimento and J. Bioucas-Dias, "Vertex component analysis: A fast algorithm to unmix hyperspectral data," *IEEE Trans. Geosci. Remote Sens.*, vol. 43, no. 4, pp. 898–910, Apr. 2005.
- [6] A. Zare and K. C. Ho, "Endmember variability in hyperspectral analysis: Addressing spectral variability during spectral unmixing," *IEEE Signal Process. Mag.*, vol. 31, no. 1, pp. 95–104, Jan. 2014.
- [7] J. M. P. Nascimento and J. M. Bioucas Dias, "Does independent component analysis play a role in unmixing hyperspectral data?" *IEEE Trans. Geosci. Remote Sens.*, vol. 43, no. 1, pp. 175–187, Jan. 2005.
- [8] C.-I. Chang, *Hyperspectral Data Exploitation: Theory and Applications*. New York, NY, USA: Kluwer, 2007.
- [9] M. E. Winter, "N-FINDR: An algorithm for fast autonomous spectral end member determination in hyperspectral data," in *Proc. SPIE Image Spectrom.*, V, 1999, vol. 3753, pp. 266–277.
- [10] C.-I. Chang, C.-C. Wu, W. Liu, and Y.-C. Ouyang, "A new growing method for simplexA new growing method for simplex-based endmember extraction algorithmbased endmember extraction algorithm," *IEEE Trans. Geosci. Remote Sens.*, vol. 44, no. 10, pp. 2804–2819, Oct. 2006.
- [11] T.-H. Chan, W.-K. Ma, A. Ambikapathi, and C.-Y. Chi, "A simplex volume maximization framework for hyperspectral endmember extraction," *IEEE Trans. Geosci. Remote Sens.*, vol. 49, no. 11, pp. 4177–4193, Nov. 2011.
- [12] M. Craig, "Minimum-volume transforms for remotely sensed data," *IEEE Trans. Geosci. Remote Sens.*, vol. 32, no. 3, pp. 542–552, May 1994.

- [13] L. Miao and H. Qi, "Endmember extraction from highly mixed data using minimum volume constrained nonnegative matrix factorization," *IEEE Trans. Geosci. Remote Sens.*, vol. 45, no. 3, pp. 765–777, Mar. 2007.
- [14] T. Chan, C. Chi, Y. Huang, and W. Ma, "Convex analysis based minimum-volume enclosing simplex algorithm for hyperspectral unmixing," *IEEE Trans. Signal Process.*, vol. 57, no. 11, pp. 4418–4432, Nov. 2009.
- [15] M. Berman *et al.*, "ICE: A statistical approach to identifying endmembers in hyperspectral images," *IEEE Trans. Geosci. Remote Sens.*, vol. 42, no. 10, pp. 2085–2095, Oct. 2004.
- [16] J. Nascimento and J. Bioucas-Dias, "Hyperspectral unmixing based on mixtures of Dirichlet components," *IEEE Trans. Geosci. Remote Sens.*, vol. 50, no. 3, pp. 695–712, Mar. 2012.
- [17] N. Dobigeon, S. Moussaoui, J.-Y. Tourneret, and C. Carteret, "Bayesian separation of spectral sources under non-negativity and full additivity constraints," *Signal Process.*, vol. 89, no. 12, pp. 2657–2669, Dec. 2009.
- [18] M. D. Iordache, J. Bioucas-Dias, and A. Plaza, "Sparse unmixing of hyperspectral data," *IEEE Trans. Geosci. Remote Sens.*, vol. 49, no. 6, pp. 2014–2039, Jun. 2011.
- [19] M.-D. Iordache, J. Bioucas-Dias, and A. Plaza, "Total variation spatial regularization for sparse hyperspectral unmixing," *IEEE Trans. Geosci. Remote Sens.*, vol. 50, no. 11, pp. 4484–4502, Nov. 2012.
- [20] C.-I. Chang and Q. Du, "Estimation of number of spectrally distinct signal sources in hyperspectral imagery," *IEEE Trans. Geosci. Remote Sens.*, vol. 42, no. 3, pp. 608–619, 2004.
- [21] C.-I. Chang, *Hyperspectral Data Processing: Algorithm Design and Analysis*. Hoboken, NJ, USA: Wiley, 2013.
- [22] J. Bioucas-Dias and J. Nascimento, "Hyperspectral subspace identification," *IEEE Trans. Geosci. Remote Sens.*, vol. 46, no. 8, pp. 2435–2445, Aug. 2008.
- [23] O. Eches, N. Dobigeon, and J.-Y. Tourneret, "Estimating the number of endmembers in hyperspectral images using the normal compositional model and a hierarchical Bayesian algorithm," *IEEE J. Sel. Topics Signal Process.*, vol. 3, no. 3, pp. 582–591, Jun. 2010.
- [24] B. Luo, J. Chanussot, S. Douté, and L. Zhang, "Empirical automatic estimation of the number of endmembers in hyperspectral images," *IEEE Geosci. Remote Sens. Lett.*, vol. 10, no. 1, pp. 24–28, Jan. 2013.
- [25] D. Heinz and C.-I. Chang, "Fully constrained least squares linear spectral mixture analysis method for material quantification in hyperspectral imagery," *IEEE Trans. Geosci. Remote Sens.*, vol. 39, no. 3, pp. 529–545, Mar. 2001.
- [26] A. Plaza, P. Martinez, R. Perez, and J. Plaza, "A quantitative and comparative analysis of endmember extraction algorithms from hyperspectral data," *IEEE Trans. Geosci. Remote Sens.*, vol. 42, no. 3, pp. 650–663, Mar. 2004.
- [27] S. Lopez *et al.*, "A new preprocessing technique for fast hyperspectral endmember extraction," *IEEE Geosci. Remote Sens. Lett.*, vol. 10, no. 5, pp. 1070–1074, Sep. 2013.
- [28] S. Bernabe *et al.*, "Hyperspectral unmixing on GPUs and multi-core processors: A comparison," *IEEE J. Sel. Topics Appl. Earth Observ. Remote Sens.*, vol. 6, no. 3, pp. 1386–1398, Jun. 2013.
- [29] S. Lopez *et al.*, "The promise of reconfigurable computing for hyperspectral imaging on-board systems: Review and trends," *Proc. IEEE*, vol. 101, no. 3, pp. 698–722, Mar. 2013.
- [30] M. Xu, B. Du, and L. Zhang, "Spatial-spectral information based abundance-constrained endmember extraction methods," *IEEE J. Sel. Topics Appl. Earth Observ. Remote Sens.*, vol. 7, no. 6, pp. 2004–2015, Jun. 2014.
- [31] S. Dowler and M. Andrews, "Abundance guide endmember selection: An algorithm for unmixing hyperspectral data," in *Proc. IEEE 17th Int. Conf. Image Process.*, 2010, pp. 2649–2652.



**Rubén Marrero** received the Engineer and M.Sc. degrees in telecommunication technologies and the Electronics Engineer degree from Las Palmas de Gran Canaria University (ULPGC), Las Palmas, Spain, in 2011, 2012, and 2013, respectively.

From 2012 and 2013, he was working on hyperspectral imaging with the Institute for Applied Microelectronics, ULPGC. Since October 2013, he has been a Researcher with Institut de Planétologie et d'Astrophysique de Grenoble (IPAG), Université Joseph Fourier (UJF), Centre National de la Recherche Scientifique, Saint-Martin-d'Hères, France. His current research interests include remote sensing, radiative transfer, and physics modeling applied to planetary science.



**Sebastian Lopez** (M'08) was born in Las Palmas de Gran Canaria, Spain, in 1978. He received the Electronic Engineer degree from the University of La Laguna, San Cristóbal de La Laguna, Spain, in 2001 and the Ph.D. degree from the University of Las Palmas de Gran Canaria, Las Palmas, Spain, in 2006.

He is currently an Associate Professor with the University of Las Palmas de Gran Canaria, developing his research activities at the Integrated Systems Design Division of the Institute for Applied Microelectronics. He is the author of more than 80 papers in international journals and conferences. His current research interests include real-time hyperspectral imaging, reconfigurable architectures, high-performance computing systems, and image and video processing.

Dr. Lopez currently serves as an Administrative Committee member of the Spanish Chapter of the IEEE Geoscience and Remote Sensing Society. He is also a program committee member for different international conferences including the SPIE Conference on Satellite Data Compression, Communication and Processing, IEEE Workshop on Hyperspectral Image and Signal Processing: Evolution in Remote Sensing (WHISPERS), and SPIE Conference of High Performance Computing in Remote Sensing. Furthermore, he acted as one of the program chairs at the last two aforementioned conferences for their 2014 editions and will be the program chair of the SPIE Conference of High Performance Computing in Remote Sensing in 2015. He served as an Associate Editor for the IEEE TRANSACTIONS ON CONSUMER ELECTRONICS from 2008 to 2013. He currently serves as an Associate Editor for the IEEE JOURNAL OF SELECTED TOPICS IN APPLIED EARTH OBSERVATIONS AND REMOTE SENSING (JSTARS) and as an active Reviewer for the IEEE JSTARS, IEEE TRANSACTIONS ON GEOSCIENCE AND REMOTE SENSING, IEEE GEOSCIENCE AND REMOTE SENSING LETTERS, IEEE TRANSACTIONS ON CIRCUITS AND SYSTEMS FOR VIDEO TECHNOLOGY, the *Journal of Real Time Image Processing, Microprocessors and Microsystems: Embedded Hardware Design*, and the *IET Electronics Letters*, among others. Moreover, he was the Guest Editor of the special issue entitled "Design and Verification of Complex Digital Systems" that was published in 2011 at the *Elsevier Microprocessors and Microsystems: Embedded Hardware Design* and is one of the guest editors of the special issue entitled "Hyperspectral remote sensing" that will be published in the IEEE JOURNAL OF SELECTED TOPICS IN APPLIED EARTH OBSERVATIONS AND REMOTE SENSING in 2015. He has received regional and national awards.



**Gustavo M. Callicó** (M'08) was born in Granada, Spain, in 1970. He received the Telecommunication Engineer degree and the Ph.D. and European Doctorate degrees from the University of Las Palmas de Gran Canaria (ULPGC), Las Palmas, Spain, in 1995 and 2003, respectively, all with honors.

For 1996–1997, he was granted with a research grant by the Ministry of Education, and in 1997, he was hired by the ULPGC as a Lecturer for electronics. In 1994, he joined the Institute for Applied Microelectronics (IUMA), ULPGC. From 2000 to 2001, he was with the Philips Research Laboratories, Eindhoven, The Netherlands, as a Visiting Scientist, where he developed his Ph.D. thesis. He is currently an Associate Professor with the ULPGC and develops his research activities at the Integrated Systems Design Division, IUMA. He has more than 50 publications in national and international journals and conferences and has participated in 16 research projects funded by the European Community, the Spanish Government, and international private industries. His current research interests include real-time super-resolution algorithms, synthesis-based design for systems-on-a-chip, real-time hyperspectral imaging systems and circuits for multimedia processing, and video coding standards.

Dr. Callicó is a member of the Consumer Electronics Society and a member of the Publications Review Committee of the IEEE TRANSACTIONS ON CONSUMER ELECTRONICS. He currently serves as an active Reviewer of the *ACM Transactions on Design Automation of Electronic Systems*, the *Electronics and Telecommunications Research Institute (ETRI)*, the *EURASIP Journal on Embedded Systems*, the *SPIE Journal of Electronic Imaging*, the *Springer Journal of Real-Time Image Processing*, and the *Elsevier Journal of Microprocessors and Microsystems: Embedded Hardware Design*.



**Miguel Angel Veganzones** (M'12) received the M.Sc. and Ph.D. degrees in computer science from the Basque Country University, Donostia, Spain, in 2005 and 2012, respectively.

Since 2012, he has been a Postdoctoral Researcher with the Images and Signal Department with the GIPSA-lab, Grenoble-INP, Grenoble, France. Since 2004, he has been working in machine learning and image processing. His current main research interests include the analysis of hyperspectral images by means of computational intelligence and statistical

techniques.

Dr. Veganzones is a Reviewer for the IEEE TRANSACTIONS ON GEOSCIENCE AND REMOTE SENSING, the IEEE GEOSCIENCE AND REMOTE SENSING LETTERS, and the IEEE JOURNAL ON SELECTED TOPICS IN APPLIED EARTH OBSERVATIONS AND REMOTE SENSING.



**Jocelyn Chanussot** (M'04–SM'04–F'12) received the M.Sc. degree in electrical engineering from the Grenoble Institute of Technology (Grenoble INP), Grenoble, France, in 1995 and the Ph.D. degree from Savoie University, Annecy, France, in 1998.

In 1999, he was with the Geography Imagery Perception Laboratory for the Délegation Générale de l'Armement (DGA—French National Defense Department). Since 1999, he has been with Grenoble INP, where he was an Assistant Professor from 1999 to 2005, an Associate Professor from 2005 to 2007,

and is currently a Professor of signal and image processing. He is conducting his research at the Grenoble Images Speech Signals and Automatics Laboratory (GIPSA-Lab). He is a member of the Institut Universitaire de France (2012–2017). Since 2013, he has also been an Adjunct Professor with the University of Iceland, Reykjavik, Iceland. His research interests include image analysis, multicomponent image processing, nonlinear filtering, and data fusion in remote sensing.

Dr. Chanussot was a member of the IEEE Geoscience and Remote Sensing Society Administrative Committee (2009–2010), in charge of membership development. He was the General Chair of the first IEEE GRSS Workshop on Hyperspectral Image and Signal Processing, Evolution in Remote sensing (WHISPERS). He was the Chair (2009–2011) and Cochair of the GRS Data Fusion Technical Committee (2005–2008). He was a member of the Machine Learning for Signal Processing Technical Committee of the IEEE Signal Processing Society (2006–2008) and the Program Chair of the IEEE International Workshop on Machine Learning for Signal Processing, (2009). He was an Associate Editor for the IEEE GEOSCIENCE AND REMOTE SENSING LETTERS (2005–2007) and for *Pattern Recognition* (2006–2008). Since 2007, he has been an Associate Editor for the IEEE TRANSACTIONS ON GEOSCIENCE AND REMOTE SENSING. He has been the Editor-in-Chief of the IEEE JOURNAL OF SELECTED TOPICS IN APPLIED EARTH OBSERVATIONS AND REMOTE SENSING since 2011. He was a Guest Editor for the PROCEEDINGS OF THE IEEE in 2013 and a Guest Editor for the IEEE SIGNAL PROCESSING MAGAZINE in 2014. He is the founding President of IEEE Geoscience and Remote Sensing Society (GRSS) French chapter (2007–2010) which received the 2010 IEEE GRSS Chapter Excellence Award. He was the coreipient of the NORSIG 2006 Best Student Paper Award, the IEEE GRSS 2011 Symposium Best Paper Award, the IEEE GRSS 2012 Transactions Prize Paper Award, and the IEEE GRSS 2013 Highest Impact Paper Award.



**Antonio Plaza** (M'05–SM'07–F'15) received the Degree, M.Sc., and Ph.D. degrees from the University of Extremadura, Extremadura, Spain, in 1997, 1999, and 2002, respectively, all in computer engineering.

He is an Associate Professor (with accreditation for Full Professor) with the Department of Technology of Computers and Communications, University of Extremadura, where he is the Head of the Hyperspectral Computing Laboratory (HyperComp).

From 2007 to 2011, he was the Coordinator of the Hyperspectral Imaging Network, a European project with total funding of 2.8 million euros. He is currently an Associate Professor (with accreditation for Full Professor) with the Department of Technology of Computers and Communications, University of Extremadura, where he is the Head of the Hyperspectral Computing Laboratory (HyperComp). He is the author of more than 370 publications, including more than 100 Journal Citation Reports (JCR) journal papers (60 in IEEE journals), 20 book chapters, and over 230 peer-reviewed conference proceeding papers (90 in IEEE conferences).

Dr. Plaza served as an Associate Editor for the IEEE TRANSACTIONS ON GEOSCIENCE AND REMOTE SENSING from 2007 to 2012. He is a Guest Editor of seven special issues on JCR journals (three in IEEE journals). He was a member of the Editorial Board of the IEEE GEOSCIENCE AND REMOTE SENSING NEWSLETTER from 2011 to 2012 and a member of the steering committee of the IEEE JOURNAL OF SELECTED TOPICS IN APPLIED EARTH OBSERVATIONS AND REMOTE SENSING in 2012. He is also an Associate Editor for IEEE ACCESS and the IEEE GEOSCIENCE AND REMOTE SENSING MAGAZINE. He is currently serving as the Editor-in-Chief of the IEEE TRANSACTIONS ON GEOSCIENCE AND REMOTE SENSING (since January 2013). He served as the Chair of the 2011 IEEE Workshop on Hyperspectral Image and Signal Processing: Evolution in Remote Sensing. He served as the Director of Education Activities for the IEEE Geoscience and Remote Sensing Society (GRSS) from 2011 to 2012, and is currently serving as President of the Spanish Chapter of IEEE GRSS (since November 2012). He received the recognition of Best Reviewers of the IEEE GEOSCIENCE AND REMOTE SENSING LETTERS in 2009 and of Best Reviewers of the IEEE TRANSACTIONS ON GEOSCIENCE AND REMOTE SENSING in 2010.



**Roberto Sarmiento** received the Ph.D. degree in electronic engineering from the University of Las Palmas de Gran Canaria, Las Palmas de Gran Canaria, Spain, in 1991.

He is a Full Professor in electronic engineering with the Telecommunication Engineering Faculty at the University of Las Palmas de Gran Canaria.

He contributed to the birth of Telecommunication Engineering Faculty, University of Las Palmas de Gran Canaria (ULPGC), Las Palmas, Spain, in 1989. From 1994 to 1998, he was the Dean of the Faculty, and from 1998 to 2003, he was the Vice Chancellor for Academic Affairs and Staff at the ULPGC. He is currently a Full Professor of electronic engineering with the Telecommunication Engineering Faculty, ULPGC. In 1993, he was a Visiting Professor with The University of Adelaide, Adelaide, Australia, and later at the University of Edith Cowan, Mount Lawley, Australia. He is a cofounder of the Institute for Applied Microelectronics, ULPGC, and the Director of the Integrated Systems Design Division of this institute. Since 1990, he has published more than 40 journal papers and book chapters and more than 120 conference papers. He has participated in more than 35 projects and research programs funded by public and private organizations, and has been a Lead Researcher in 16 of them. He has conducted several agreements with companies for the design of high-performance integrated circuits, being the most remarkable the collaboration with Vitesse Semiconductor Corporation, CA, USA and Thales Alenia Space, Spain. His research interests include multimedia processing and video coding standard systems, reconfigurable architectures and real-time processing, and compression of hyperspectral imaging.

Dr. Sarmiento has been awarded with four six-year research periods by the National Agency for the Research Activity Evaluation in Spain.